




A wearable and stretchable dual-wavelength LED device for home care of chronic infected wounds

Received: 18 June 2024

Accepted: 16 October 2024

Published online: 30 October 2024

Ming Li^{1,2,4}, Chenxi Wang^{2,4}, Qiang Yu², Haoyi Chen², Yingying Ma², Li Wei², Mei X. Wu^{3,5}  , Min Yao^{1,5}   & Min Lu^{2,5}  

Phototherapy can offer a safe and non-invasive solution against infections, while promoting wound healing. Conventional phototherapeutic devices are bulky and limited to hospital use. To overcome these challenges, we developed a wearable, flexible red and blue LED (r&bLED) patch controlled by a mobile-connected system, enabling safe self-application at home. The patch exhibits excellent skin compatibility, flexibility, and comfort, with high safety under system supervision. Additionally, we synthesized a sprayable fibrin gel (F-gel) containing blue light-sensitive thymoquinone and red light-synergistic NADH. Combined with bLED, thymoquinone eradicated microbes and biofilms within minutes, regardless of antibiotic resistance. Furthermore, NADH and rLED synergistically improved macrophage and endothelial cell mitochondrial function, promoting wound healing, reducing inflammation, and enhancing angiogenesis, as validated in infected diabetic wounds in mice and minipigs. This innovative technology holds great promise for revolutionizing at-home phototherapy for chronic infected wounds.

With an aging population and increasing rates of diabetes, obesity, and systemic disease, non-healing chronic wounds, including diabetic foot ulcers, venous leg ulcer wounds, and pressure ulcers, pose an imminent threat to the global economy and medical system^{1–3}. Upon disruption of the protective skin barrier, the wound bed and underlying tissue provide a natural and fertile environment for microbial growth. Microbial colonization, biofilm formation, and infection can all hinder the wound healing process and result in serious complications such as osteomyelitis, amputation, or, in extreme cases, death⁴. The use of antibiotics is a common treatment for infected chronic wounds⁵. However, the overuse, misuse, and abuse of antibiotics have led to a significant escalation of microbial resistance, resulting in a sharp increase in treatment cost, duration, and patient mortality rate^{6,7}. In

addition, pathological conditions like diabetes prevent macrophages from entering repair mode, causing prolonged inflammation and delayed wound healing⁸. This leads to oxidative stress in endothelial cells and disruption of wound vascularization, crucial for healing^{9,10}. Targeting macrophage repolarization and enhancing vascularization are promising strategies for chronic wound treatment¹¹. Therefore, combating microbial infection and facilitating wound healing are both critical to the management of chronic wounds.

Safe and non-invasive phototherapy has received increasing attention in chronic wound care. Photodynamic therapy (PDT) and photobiomodulation (PBM) are emerging as promising options for combating microbial infection and facilitating wound healing, respectively. Blue light has been investigated for its safe, efficient, and

¹Department of Plastic and Reconstructive Surgery, Shanghai Ninth People's Hospital, Shanghai Jiao Tong University School of Medicine, Shanghai 200011, China. ²Department of Orthopaedics, Shanghai Key Laboratory for Prevention and Treatment of Bone and Joint Diseases, Shanghai Institute of Traumatology and Orthopaedics, Ruijin Hospital, Shanghai Jiao Tong University School of Medicine, Shanghai 200025, China. ³Wellman Center for Photomedicine, Massachusetts General Hospital Department of Dermatology, Harvard Medical School, 50 Blossom Street, Boston, MA 02114, USA. ⁴These authors contributed equally: Ming Li, Chenxi Wang. ⁵These authors jointly supervised this work: Mei X. Wu, Min Yao, Min Lu. ✉ e-mail: mwu5@mgh.harvard.edu; minyao@sjtu.edu.cn; lumin111@sjtu.edu.cn

broad-spectrum antibacterial properties, as it can effectively eliminate a variety of bacteria, irrespective of antibiotic susceptibility^{12,13}. In addition, PBM employs red or near-infrared (NIR) light to stimulate the dissociation of NO from Complex IV (CIV, cytochrome c oxidase), a key rate-limiting enzyme of the electron transport chain (ETC), or directly activates CIV, leading to the alterations in oxidative stress within mitochondria. This process enhances oxidative phosphorylation (OXPHOS) and accelerates the mitochondrial respiratory chain (MRC) in cells under stress, resulting in improved mitochondrial functions and wound healing^{14,15}. Various phototherapies have been practiced for decades demonstrating beneficial effects in hospital settings as phototherapies can be targeted to specific tissues or organs, enabling the practice of precision medicine¹⁶. However, conventional phototherapeutic devices are burdened by their large size, depending on specialized operators, high treatment costs, user-unfriendly treatment, and the inability to accommodate various wound shapes during therapy. These limitations hinder their broad application at home.

In recent years, flexible and wearable body-conforming electronics have been increasingly developed in various fields, such as energy harvesting and storage, health sensing, monitoring, etc. These electronics are characterized by their flexibility, stretchability, and softness, allowing them to be seamlessly and discreetly integrated into the human body to carry out various tasks^{17–19}. LED light source technology has developed rapidly in recent years, but the advancement of flexible LED phototherapy devices for home use has encountered numerous obstacles. Micro-LEDs and OLEDs exhibit superior light extraction efficiency and reduced self-heating compared to traditional LEDs^{20,21}. In addition, quantum dot light-emitting diodes (QD-LEDs) and QD-OLED are among the most promising self-emitting displays in terms of luminous efficiency, wavelength tunability, and cost^{22,23}. Moreover, metal halide perovskites are attracting considerable attention as next-generation light-emitting materials due to their exceptional emission characteristics, with narrow-band emission²⁴. As of now, Micro-LED technology is still emerging and hasn't been widely adopted in FDA-approved home medical devices. The technology's high cost and early stage of development have limited its use primarily to consumer electronics and high-end displays, rather than medical applications at home²⁵. Additionally, despite significant advances in OLED technology and improvements in OLED lifespan, achieving stable and efficient blue OLEDs remains a challenge^{26,27}. Improving OLEDs with stability and high efficiency is crucial for developing multi-wavelength OLED phototherapy devices that require long-term, high-performance, and stable operation, especially for treating open chronic wounds. Traditional LEDs are known for their high stability, long lifespan, and excellent monochromaticity^{28,29}. In addition, traditional LEDs have been approved by the FDA for medical devices and have demonstrated their safety in clinical applications and home³⁰. Therefore, flexible LED phototherapy devices are primarily reliant on traditional LED chips as of today. Lee, So Yun et al. developed a wearable LED patch based on polyimide (PI) substrate for PBM in wound healing, improving the convenience of treatment³¹. However, the PI substrate lacks stretchability, the patch emits only red light, and it is unable to address infected wounds. To create stretchable LED devices with non-stretchable traditional LED chips, the island-bridge structure with serpentine interconnects, wavy buckling, and kirigami-/origami-inspired structures were employed by researchers. Hu et al. developed a stretchable inorganic semiconductor electronic system via an island-bridge structure³². Yusuke et al. developed a stretchable kirigami structure based on 10- μ m-thin polyimide membranes comprising LED chips and microelectrodes for optophysiological experiments in perfused hearts³³. However, these designs often require complex manufacturing processes, making it difficult to achieve the high power density required for phototherapy. In addition, these designs do not take it into account the convenience of home use, and no devices have been developed for home phototherapy of open wounds.

To address these challenges, we developed a wearable phototherapy device for home use, employing a straightforward manufacturing process. This device not only ensures the required power density, treatment stability, and stretchability for effective phototherapy but also provides the convenience at-home treatment (Fig. 1a). The device consists of a dual-wavelength red and blue LED (r&bLED) patch and an intelligent control module, enabling users to control devices via a mobile phone at home (Fig. 1b). The patch boasts a multi-layer structure, including substrate, interconnectors, temperature sensor and r&bLED chips, a PDMS encapsulation layer on the top and a reflective layer on the back (Fig. 1c). The patch is flexible, stretchable, and deformable to conform to body contours for uniform light delivery, real-time temperature monitoring prevents thermal skin damage during therapy, and its anti-microbial adhesion and waterproof design ensures longevity (Fig. 1d). The patch is controlled by an intelligent system, akin in size to an AirPods charging box, wirelessly connected to a mobile phone, with a lithium battery for up to 2–3 hrs of continuous use (Supplementary Fig. 1).

In this work, to enhance the therapeutic efficacy of the r&bLED patch, blue light-sensitive thymoquinone (TQ) and red light-synergistic reduced nicotinamide adenine dinucleotide (NADH) were added to a sprayable fibrin gel (F-gel), which is highly compatible to the skin, forming a thin film readily on the skin (Fig. 1e,f). When F-gel was spread onto the wound, followed by r&bLED patch application with the light on, the dual-functionality of anti-infection and wound healing acceleration via mitochondrial improvement was achieved with much shortened illumination (Fig. 1e,g). The effectiveness of the device in combination with F-gel in eliminating microbial infections and expediting wound healing was validated in infected diabetic wounds in both mice and minipigs (Fig. 1h). The remarkable efficiency is largely attributed to improved mitochondrial functions in macrophages and endothelial cells, resulting in favorable macrophage polarization, suppression of inflammatory, and promotion of angiogenesis. The device shows immense potential as a revolutionary at-home optical treatment of infected chronic wounds.

Results

Preparation and characterization of the r&bLED patch and control module

To address the limited stretchability of the polyimide (PI) substrate³¹ and increase skin biocompatibility, thermoplastic polyurethane (TPU) with exceptional elasticity and mechanical properties was used as a substrate in our study, critical qualities for wearable devices (Fig. 2a). To accommodate various wound shapes and sizes in cost-effective mass production, the circuits are manufactured using the well-established dispensing printing process, ideal for manufacturing a diverse range of circuits at a low cost. Silver nanowires (AgNW) with good tensile stability and electrical conductivity were put on both sides using the dispensing printer. PBM and PDT frequently employ light of varying wavelengths. To streamline users' experience and eliminate the need for switching between patches with different wavelengths, we combined the functional designs for PBM and PDT into a single patch. After applying a high-density conductive silver paste, packaged red LED (rLED) chips (wavelength = 630 nm, typical wavelength for PBM) and blue LED (bLED) chips (wavelength = 470 nm, typical wavelength for PDT) with a temperature sensor were manually fitted on the substrate, and then a reflow process was performed at a temperature of 90 °C with a melting interval duration of 3 min, ensuring the stability of LED chips and temperature sensor. Subsequently, the chips and interconnects constructed on TPU were readily encapsulated with thin layers of transparent polydimethylsiloxane (PDMS) to safeguard against infiltration by biological fluids and microbial adhesion. To prevent light escaping from the back and exposure of the eyes to the light, we coated the patch with PDMS combined with reflective paint, which not only prevents

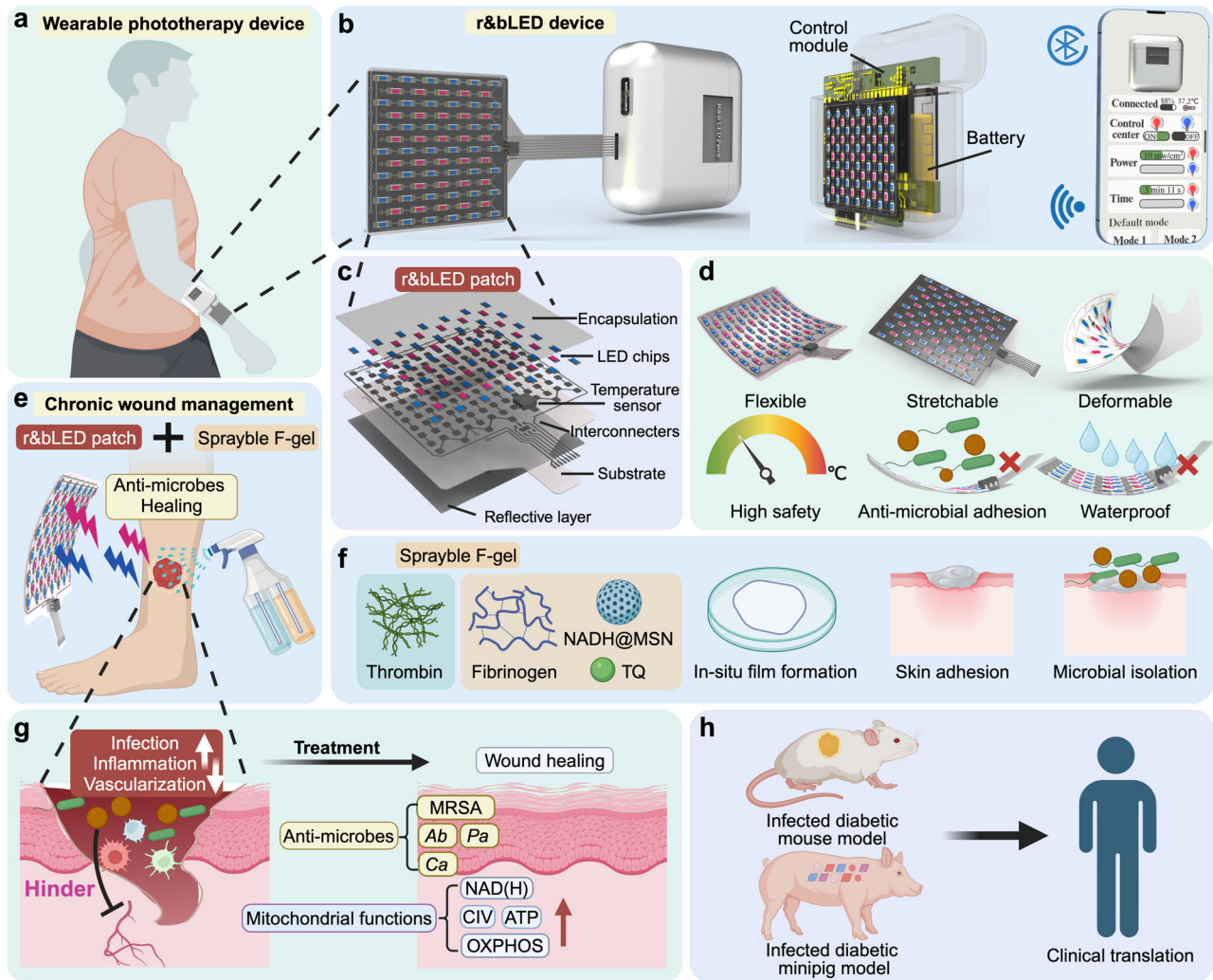


Fig. 1 | A wearable r&bLED patch combined with sprayable fibrin gel for wound treatment. **a** The application diagram of wearable phototherapy device. **b** Schematic diagram of wearable r&bLED patch and control module. **c** Structure of the r&bLED patch. **d** Characterization of r&bLED patch. **e** Schematic illustration of the combinatory treatment for the management of chronic wound. **f** Constitution

and characterization of F-gel. **g** Efficacy of the combination treatment. **h**, Validation of the diabetic wound healing efficacy based on in vivo infected diabetic mouse model and in vivo infected diabetic minipig models. This figure was created with BioRender.com released under a Creative Commons Attribution-NonCommercial-NoDerivs 4.0 International license.

light transmission but also boosts light usage and homogeneity. The paper-like r&bLED patch is manufactured in a customizable size, and the aggregate thickness after encapsulation was only ~600 μm (Fig. 2a).

As shown in Fig. 2b and Supplementary Fig. 2a, the r&bLED patch is capable of emitting either monochromatic or bichromatic light, facilitated by the separate circuit for rLED and bLED chips. The patch showed power densities of bLED and rLED were 42.1 mW/cm^2 and 10.3 mW/cm^2 , respectively, when the forward current was 20 mA, and the power densities did not significant decrease after PDMS encapsulation (Fig. 2c). The low operating voltage of the chips ensures the electrical safety of the r&bLED patch when applied to skin or tissue and small batteries could serve as power sources for the patch (Fig. 2d). Moreover, the power densities of bLED and rLED can reach 55 mW/cm^2 and 16 mW/cm^2 when the forward current was adjusted to 25 mA (Fig. 2e), which can readily achieve the ideal power for PDT and PBM, enabling the r&bLED patch for effective phototherapy^{12,31}. We set the power densities of bLED and rLED to 50 mW/cm^2 and 10 mW/cm^2 for the following experiments. Notably, the optical power density uniformity reached approximately 69% and 71% for rLED and bLED, respectively, due to the dense arrangement of rLED and bLED chips

(Fig. 2f). When the density of the LED chips was reduced to 50% of the intended level, the uniformity of the light drops to 19.6% and 26.0% for rLED and bLED, respectively (Supplementary Fig. 2b).

The superior elasticity and excellent mechanical strength of TPU and AgNW facilitated the r&bLED patch with flexibility and stretchability (Fig. 2g, Supplementary Fig. 2c,d, and Supplementary video 1, 2). The patch exhibited outstanding mechanical stability during repetitive folding and stretching tests conducted under various bending radii and stretch percentages. The power densities and corresponding characteristics were measured at specific radius curvatures ranging from 50 to 10 mm and stretch percentages from 100% to 150%, as illustrated in Fig. 2h and i, respectively. The power density remains stable as the patch is bent, but it decreases ignorantly in proportion to the strain as the patch is stretched. As the LED patch stretch percentage increases, the average power density measured by the optical power meter tends to decrease, dropping by approximately 35% at 150% stretch. In addition, the uniformity of the optical power density decreased when the patch was stretched (Supplementary Fig. 2e). Moreover, the power density of the patch is still stable after 1000 bending cycles (Fig. 2j), with only 5% attenuation after 1000 stretch cycles (Fig. 2k) due to the ideal stretchable

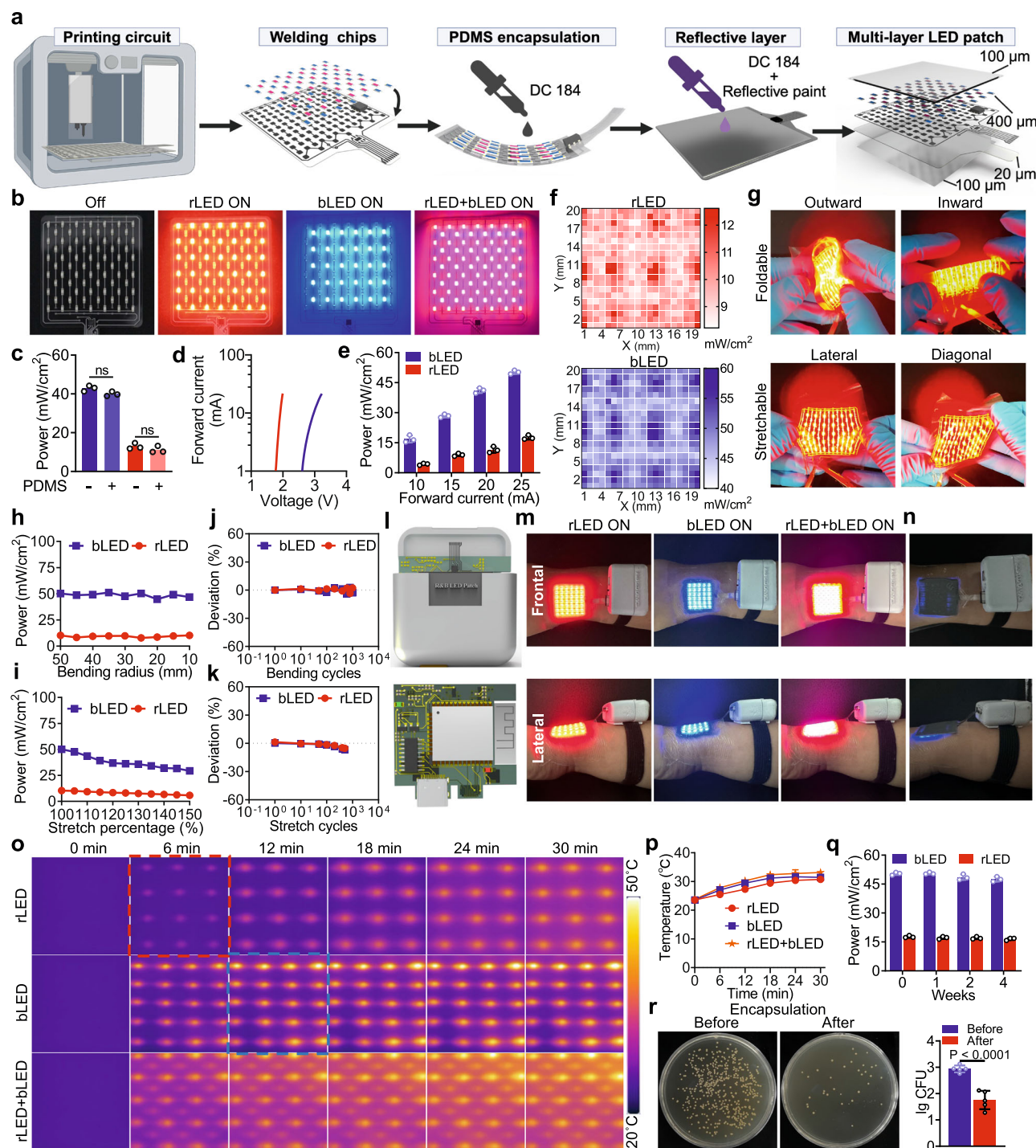


Fig. 2 | Preparation and characterization of r&bLED patches. **a** Schematic illustration of the preparation of flexible r&bLED patches. **b** Real picture of r&bLED patch with LED ON or OFF. **c**, Optical power density of the r&bLED patch encapsulated with PDMS or not ($n = 3$ independent patches in each group). **d** Current/voltage characteristics of the LED chips in r&bLED patches. **e** Adjustable optical power density of the r&bLED patch by the control of forward current of LED chips ($n = 3$ independent patches in each group). **f** Optical power density distribution heatmap of rLED and bLED. **g** Real pictures of r&bLED patch show the stretching and folding properties. **h**, **i**, Power density versus bending radius (**h**) and stretch percentage (**i**) plot of rLED and bLED. **j**, **k** Power density deviation percentage versus bending (**j**) and stretch (**k**) cycles plot of rLED and bLED. **l**, Photographs of portable phototherapy device and control module. **m**, r&bLED patch fits on the

wrist. **n**, Pictures of r&bLED patch after encapsulated with PDMS mixed with reflective paint. **o**, **p** Thermal imaging photos of r&bLED patch with LED chips turned on (**o**) and temperature-time curve (**p**) ($n = 3$ independent patches in each group). **q** Power density of bLED and rLED after immersion in PBS for different time ($n = 3$ biologically independent samples in each group). The forward current was adjusted to 25 mA. **r** Residual bacteria in cotton swab after scraping the patch (before or after encapsulation) exposed to suspension containing MRSA ($n = 5$ biologically independent experiments per group). Data are presented as mean values \pm SEM. Statistical significance and P values were determined by two-tailed t test was used in **a** and **r**. Panel **a** was created with BioRender.com released under a Creative Commons Attribution-NonCommercial-NoDerivs 4.0 International license.

properties of TPU substrate and AgNW. The excellent stretch and bending stability of the r&bLED patch ensures the reliability of household applications.

To enable control over LED switches, power density selection, and real-time temperature monitoring of the treatment area, an intelligent control system were designed to be compact, similar in size to an AirPods charging box, and linked to the r&bLED patch using a flexible printed circuit (FPC) connector (Fig. 2l and Supplementary Fig. 1). The control system communicates with the computer via a type-C interface, and the program can be modified in the computer to calibrate the forward current and a corresponding optical power of r&b LED patch. In case the treatment temperature surpasses 42 °C (the designated safe temperature limit), a warning buzzer integrated into the control system can sound an alarm, prompting the circuit to automatically power off. Moreover, the FCP connector enables the control system to connect r&bLED patches in various sizes customized to the wounds of patients. In addition, the intelligent control system offers connectivity options via Bluetooth or Wi-Fi, enabling users to monitor the patch's temperature in real-time and adjust the power density and duration of the light irradiation conveniently through their mobile phones at home (Supplementary Fig. 1 and Supplementary video 3). A wearable device should possess excellent skin compatibility and flexibility³⁴. Due to the exceptional biocompatibility of PDMS, prolonged wear of the LED patch for several hours or even a whole day does not induce any observable skin reactions (Supplementary Fig. 2f). The r&bLED patch can adhere closely to the skin, even on joints like the wrist (Fig. 2m) and finger (Supplementary Fig. 2g), warranting precise and effective illumination even during joint movements (Supplementary video 4, 5). The patch can be applied to tissue while the animal is moving or sedated, further demonstrating its suitability as a wearable system (Supplementary video 6). The r&bLED patch allows patients to move freely during treatment and receive treatment at home, greatly improving the comfort and convenience of phototherapy. To prevent light escape from the patch and increase the utilization and uniformity of light, the back of the substrate is coated with PDMS mixed with reflective paint (Fig. 2n).

The safety caused by electric-light-thermal conversion was also determined when monochromatic or bichromatic light was on. The average temperature reached -30 °C after turning rLED, bLED, or both on for 30 min, which is much longer than the treatment time needed (Fig. 2o, p). Moreover, the hydrophobic PDMS encapsulation facilitated the patch with ideal water resistance, and the power densities of rLED and bLED chips remained stable after immersion in PBS for 4 consecutive weeks (Fig. 2q). Additionally, residual bacteria significantly decreased after PDMS encapsulation when exposed to MRSA suspension due to the smooth surface and anti-adhesion property of the patch (Fig. 2r). The aforementioned stretchability, durability, comfortability, and biosafety of the r&bLED patch make it an ideal portable device for friendly household uses.

Fabrication and characterization of sprayable and in-situ formed fibrin gel

To enhance the treatment efficacy and shorten illumination time, FDA-approved sprayable and in-situ formed fibrin gel (F-gel) was synthesized and embedded with blue light photosensitizer and NADH, an enhancer for mitochondrial function. F-gel exhibits a gentle texture, retains sufficient moisture, and serves as a protective barrier against bacterial infections, an ideal hydrogel matrix for household wound care³⁵. Moreover, its efficient drug delivery capability further establishes it as the preferred choice for wound management^{35,36}. The mesoporous silica nanoparticles (MSNs) were prepared by a sol-gel process under base catalysis, as reported³⁷, mixed with NADH solution, and incubated at 25 °C for 2 hrs to form NADH@MSNs. The loading efficiency and content of NADH@MSNs were 53.6% and 8.9%, respectively. The F-gel was prepared by spraying equal volumes of fibrinogen

(10 mg/mL) and thrombin (10 U/mL), which rapidly formed a film-like hydrogel in a dish or on hand within 120 seconds (Fig. 3a and Supplementary Fig. 3a). Integral formation of gel on hand suggests ideal skin adhesion. FTIR spectroscopy confirmed the successful drug co-loading of TQ and NADH, as indicated by the characteristic C=O and P=O peaks that appeared in the F-gel sample (Supplementary Fig. 3b). Scanning electron microscopy (SEM) revealed a distinct porous fibrin network structure in F-gel (Fig. 3b), indicating excellent air permeability and drug loading capability. The rheological test results showed that the storage modulus (G') and loss modulus (G'') of the F-gel distinctly increased over time, indicating successful gelation between fibrinogen and thrombin (Fig. 3c). Moreover, G' of the F-gel was always greater than G'' throughout the frequency domain, indicating excellent hydrogel properties (Fig. 3d). As revealed by the time-release curve of TQ and NADH from F-gel, approximately 75% of TQ was swiftly released within 20 min, whereas NADH was liberated from NADH@MSNs over a period of 4 hrs from F-gel formulated in PBS, demonstrating sustained release efficacy (Fig. 3e).

The absorption spectrum of TQ is mainly located in the regions of blue and ultraviolet (Fig. 3f), and has a good intersection with bLED chips, enabling the combinatory treatment of bLED and TQ. Meantime, the absorption spectrum of NADH does not overlap with the spectra of rLED or bLED chips, ensuring that it is not quenched and deactivated after r&bLED irradiation (Fig. 3f). In addition, the excitation spectrum of TQ shows a peak at 481 nm, which is close to the peak of bLED chips at 470 nm, whereas the excitation spectrum of NADH is not observed in the range from blue to near-infrared region (Fig. 3g). The fabricated F-gel still retains the fluorescence property of TQ, which can be specifically excited by bLED but not rLED (Fig. 3h).

Hydroxyl radical ($\cdot\text{OH}$) and hydrogen peroxide (H_2O_2) generations were further ascertained, which are primarily responsible for bactericidal activity. Both H_2O_2 (Fig. 3i) and $\cdot\text{OH}$ (Fig. 3j) productions increased significantly in the presence compared to the absence of bLED irradiation. Blue light may additionally induce H_2O_2 photolysis, further increasing $\cdot\text{OH}$ formation, and thereby the bactericidal efficacy, as $\cdot\text{OH}$ exhibits greater toxicity to bacteria than H_2O_2 ^{12,38}. The levels of $\cdot\text{OH}$ elevated significantly with increasing H_2O_2 concentrations and duration of bLED exposure (Supplementary Fig. 3c). The generations of various ROS were further detected by electron paramagnetic resonance (EPR), both $\cdot\text{OH}$ and superoxide radicals ($\text{O}_2\cdot^-$) showed clear signals, while there was no obvious signal for singlet oxygen ($^1\text{O}_2$) (Fig. 3k), suggesting the hypoxia-tolerant type I photodynamic reaction primarily occurred^{39,40}.

The transparency of F-gel is an important parameter for phototherapy efficacy. At a thickness of 4 mm, approximately 93% of red light and 85% of blue light could penetrate through the F-gel, showing excellent light transmittance (Fig. 3l). Moreover, the F-gel can uniformly coat the r&bLED patch's surface and be readily peeled off integrally, demonstrating its compatibility with the r&bLED patch for combined application (Fig. 3m,n).

ROS produced by TQ under bLED excitation can potentially harm to normal tissues. To mitigate the detrimental effects, NADH was incorporated into the F-gel because NADH is known as an antioxidant for cells and can prevent inflammation-induced cellular dysfunction and cell death^{41,42}, as illustrated in Fig. 3o. Indeed, bLED irradiation significantly reduced cell viability in the presence of TQ@F-gel, whereas cell viability was well protected when NADH was added to the F-gel and incubated prior to bLED exposure (Fig. 3p). The ROS detection further confirmed the antioxidant properties of NADH in cells during PDT, minimizing damage to normal tissue during treatment (Fig. 3q,r). The convenience of application, optimal drug-loading capacity, and excellent light transmission of F-gel, along with its ability to be sprayed and molded in place, present a great potential for synergistic use with r&bLED patch for household wound care.

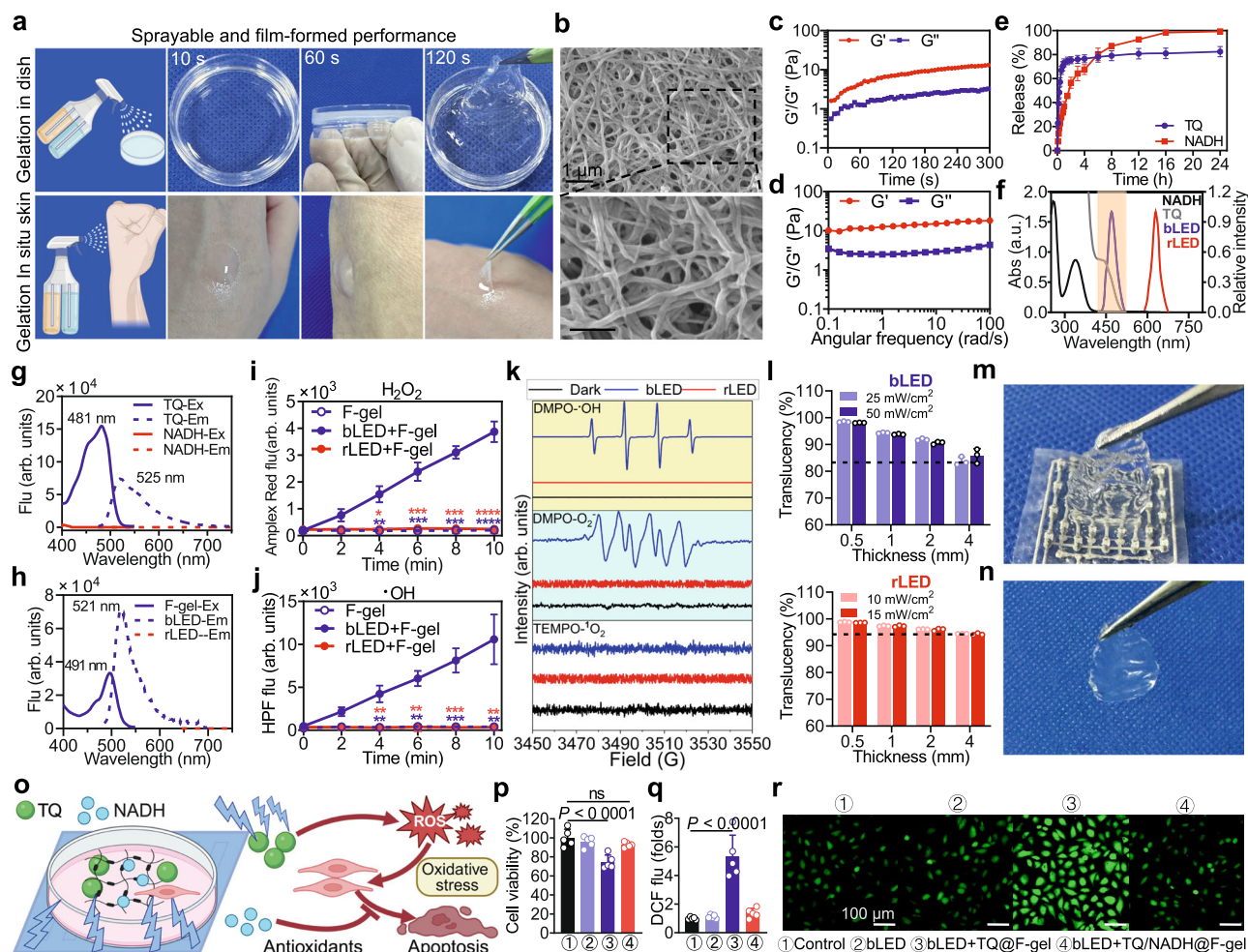


Fig. 3 | Characterization of the sprayable and in-situ formed fibrin gel. **a** Pictures show sprayable and film-formed performance of F-gel. **b**, Representative scanning electron micrographs of F-gel. **c, d**, Rheological properties of F-gel. **e** Release profile of TQ and NADH from F-gel ($n = 3$ biologically independent samples). **f** Absorption spectra of TQ, NADH and spectrum of rLED and bLED. **g, h** Excitation and emission spectra of TQ, NADH (g) and F-gel (h). **i, j**, H_2O_2 (i) and $\cdot\text{OH}$ (j) were generated by F-gel in combination with bLED ($n = 5$ biologically independent samples in each group). **k**, $\cdot\text{OH}$, $\text{O}_2^{\cdot-}$ or $\cdot\text{O}_2$ adducts identified and measured by EPR. **l** Transmittance of F-gel ($n = 3$ biologically independent samples in each group). **m, n** Adhesive properties of F-gel. **o**, Schematic illustration of the protective effect of NADH on

cells during PDT. **p**, Cell viability of HUVECs after different treatments ($n = 5$ biologically independent samples in each group). **q, r** Statistical analysis (q) and representative graphs (r) of intracellular ROS ($n = 5$ biologically independent samples in each group). Data are presented as mean values \pm SEM. Statistical significance and P values were determined by two-way ANOVA followed by Dunnett's multiple comparison test (i, j) or one-way ANOVA followed by Tukey's multiple comparison test (p, q). Parts of panel a and panel o was created with BioRender.com released under a Creative Commons Attribution-NonCommercial-NoDerivs 4.0 International license.

In vitro antimicrobial effect and mechanism of action by combination of r&bLED and F-gel

To evaluate the synergistic effects between r&bLED patch and F-gel, four common strains associated with chronic wounds, including 3 multidrug-resistant bacteria of G^+ MRSA and G^- *Pa* and *Ab*, as well as 1 fungi of *Ca* were employed (Supplementary Table 1). The procedures and rationale behind the study are illustrated in Fig. 4a. The microbial suspension at 10^7 CFU/mL in PBS was added to a 35 mm dish together with F-gel at a final concentration of TQ at 25, 50, 75, and 100 $\mu\text{g/mL}$ and then incubated for 20 min, followed by r&bLED patch exposure through the bottom of the dish. With the help of TQ, $\text{O}_2^{\cdot-}$ was generated under bLED irradiation in abundance and further reacted to form HO_2^{\cdot} and H_2O_2 , which was subsequently photolyzed to highly toxic $\cdot\text{OH}$ under the same bLED exposure (Fig. 4a). As shown in Fig. 4b, at TQ concentration of 100 $\mu\text{g/mL}$ and bLED illumination at 30 J/cm^2 , MRSA, *Pa*, and *Ab* each at a concentration of 10^7 CFU/mL, were completely eradicated, while *Ca* exhibited a reduction of 6.6 lg CFU/mL. In addition, rLED illumination or rLED combined with F-gel showed no bactericidal effect, confirming that the bactericidal effect is mediated by

bLED (Supplementary Fig. 4). The synergistic eradication of MRSA, *Ab*, *Pa*, and *Ca* was further validated via Bliss independence model, where S values across all combinations exceeded 0, with synergy levels increasing along with the enhancement of bLED doses and TQ concentrations (Fig. 4c). Among the 80 combinations tested, the mean and median were 0.410 and 0.334, respectively, indicating synergy in the combination therapy (Fig. 4d).

The bLED in combination with F-gel exhibited a higher efficacy in damaging cell envelopes compared with either treatment alone, as determined by SYTOTM 9 and propidium iodide (PI) staining (Supplementary Fig. 5 to 8). The proportion of PI-positive (PI^+) cells increased to 96%, 97%, 99%, and 93% for MRSA, *Pa*, *Ab*, and *Ca*, respectively, following a lethal dose of the combined treatment. In contrast, fewer PI^+ cells were observed when treated with either bLED or F-gel alone (Supplementary Fig. 5 to 8). The cellular alterations were ultrastructurally confirmed with SEM and transmission electron microscope (TEM) showing broken or damaged cell envelopes of MRSA, *Pa*, *Ab*, and *Ca* (Fig. 4e, f and Supplementary Fig. 9). The damages likely occurred both cell wall and cell membrane, as indicated by the

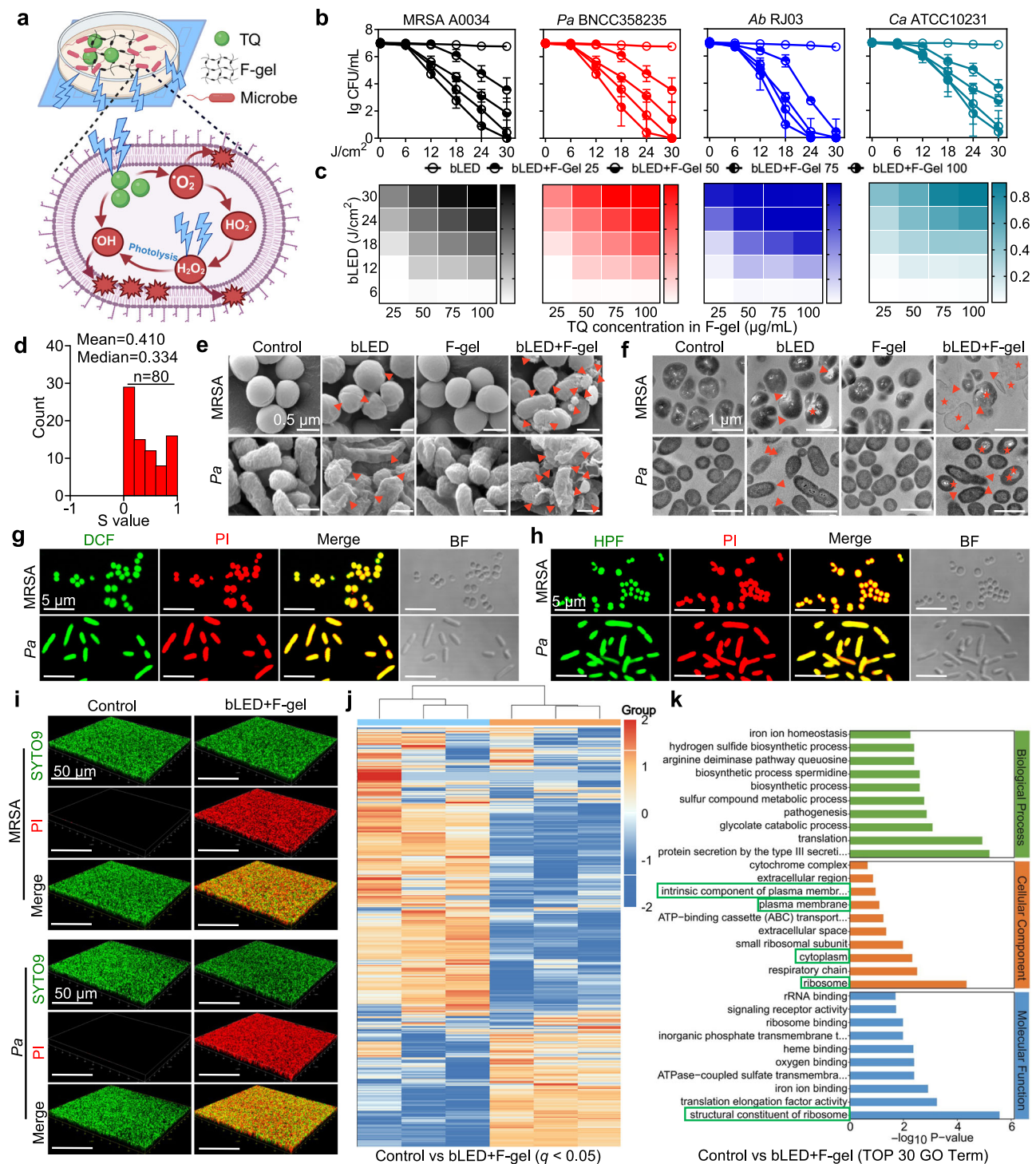


Fig. 4 | In vitro antimicrobial effect and mechanism of action by combination of r&bLED patch and F-gel. **a** Schematic illustration of the experimental design and antimicrobial mechanism. **b**, Killing curves of indicated bacterial strains in planktonic cultures ($n = 5$ biologically independent samples in each group). **c** Checkerboards for synergistic interactions between bLED and F-gel against indicated bacterial strains in planktonic cells. **d**, Distribution plot of S values. **e**, **f** Representative scanning electron micrographs (**e**) and transmission electron micrographs (**f**) of MRSA and *Pa* with or without treatment of bLED (30 J/cm²) and F-gel (final TQ concentration, 100 μg/mL). Arrows indicate bacterial envelope damage, asterisks indicate vacuoles and bubbles in cells. **g**, **h** Representative fluorescence images of the planktonic cells from MRSA (upper) and *Pa* (bottom) after combinatory treatment of bLED (30 J/cm²) and F-gel (final TQ concentration,

100 μg/mL). Bacterial intracellular ROS and \cdot OH were evaluated by H₂DCFDA (**g**) and HPF (**h**) staining, respectively, and bacterial viability was evaluated by PI staining. **i**, Confocal images and corresponding 3D images of SYTOTM 9 (green) and PI (red) stained mature biofilms after different treatments (bLED, 60 J/cm²; final TQ concentration of F-gel, 100 μg/mL). **j**, Heat map of the expressed genes of *Pa* after treatment with PBS and bLED (15 J/cm²) with F-gel (final TQ concentration, 100 μg/mL) (fold change ≥ 2 and $q < 0.05$). **k** Functional classification of the differentially expressed genes between PBS group and bLED with F-gel group by GO enrichment analysis. Data are presented as mean values \pm SEM. Panel **a** was created with BioRender.com released under a Creative Commons Attribution-NonCommercial-NoDerivs 4.0 International license.

presence of cell envelope damage (arrows) and cytoplasmic leakage (asterisks) in a significant number of MRSA and *Pa*. In contrast, untreated MRSA, *Pa*, *Ab*, and *Ca* displayed intact and smooth cell envelopes (Fig. 4e,f). In addition, the merged yellow color resulting from the combination of ROS-specific 2',7'-dichlorofluorescein (DCF) (Fig. 4g) or $\cdot\text{OH}$ -specific hydroxyphenyl fluorescein (HPF) (Fig. 4h) and PI staining provided evidence of ROS or $\cdot\text{OH}$ formation within MRSA and *Pa*, followed by a lethal dose of the combined treatment, suggesting the cell death were mainly caused by ROS generated from combinatory treatment. More importantly, in the presence of the $\cdot\text{OH}$ scavenger DMSO⁴³ or the $\text{O}_2^{\cdot-}$ scavenger Tiron⁴⁴, the bactericidal ability of the combined treatment is significantly reduced, while the presence of NaN_3 , a scavenger of $^1\text{O}_2$, does not significantly affect the antibacterial effect, further demonstrating that the antimicrobial effect is typically triggered by type I photodynamic reaction (Fig. 4a and Supplementary Fig. 10a–f). Additionally, in a hypoxic environment, DCF or HPF and PI double-staining confirmed the generation of ROS and $\cdot\text{OH}$, leading to bacterial death (Supplementary Fig. 10g,h). Similarly, mature biofilms of MRSA and *Pa* were entirely eradicated following 20 min of bLED exposure in conjunction with F-gel, as confirmed by live/dead staining (Fig. 4i), crystal violet staining (Supplementary Fig. 11a,b) and CFU measurement (Supplementary Fig. 11c). In addition, the generation of $\cdot\text{OH}$ under bLED irradiation was further demonstrated by HPF and PI staining in biofilms of MRSA and *Pa* (Supplementary Fig. 12).

To further elucidate the mechanism underlying the synergistic antimicrobial effects, transcriptome sequencing (RNA-seq) analysis was performed on *Pa*, a typical skin infection bacterium, with or without combined treatment. A total of 1055 genes were significantly and differentially expressed between the two groups (fold change ≥ 2 and $q < 0.05$) (Fig. 4j). As shown in Fig. 4k, the Gene Ontology (GO) database was used to identify the genes differentially expressed at significant levels in biological functions, revealing an increase in terms related to cellular components such as plasma membrane, cytoplasm and ribosome (green rectangle), indicating the significant impact of combined treatment on cellular component integrity. Additionally, Kyoto Encyclopedia of Genes and Genomes (KEGG) pathways and Gene Set Enrichment Analysis (GSEA) highlighted the down-regulation of genes associated with bacterial chemotaxis (like *nahY*, *STM3577*, *EAE15525*, *PP1228*, *PA0175*, *PA1459*), flagellar assembly (like *PA1104*, *STM1183*, *b1942*, *BSU13690*, *BSU29720*) and biofilm formation (like *MXAN_5788*, *PA3622*, *PA3105*, *PA3103*, *TTHA1437*) (Supplementary Fig. 13). Bacterial chemotaxis involves bacteria moving towards beneficial chemicals and away from harmful ones using flagella, and biofilms help bacteria survive in harsh environments, making them harder to eliminate, while down-regulation of certain genes indicates reduced pathogenicity of *Pa* after combined treatment^{45,46}. Therefore, the combination of r&bLED and F-gel offers a convenient, rapid, and effective sterilization manner for the management of infected wound healing at home.

r&bLED together with F-gel synergistically accelerates angiogenesis via improving MRC

PBM has been consistently shown able to increase mitochondrial functions in various cells under stress^{31,47}. Red light or NIR can activate complex IV along the mitochondrial respiratory chain (MRC), increasing the production of adenosine triphosphate (ATP) in a manner less-independent on oxygen levels^{48,49}. NADH serves as a hydrogen donor and plays a crucial role in maintaining the integrity of electron transport chain (ETC) and MRC⁵⁰. Therefore, PBM and NADH may exhibit a synergistic effect in improving mitochondrial function. Indeed, a combination of rLED and NADH synergistically enhanced ETC flux and MRC by rebuilding NAD(H) reservoir and elevating CIV activity, further enhancing ATP production, thereby promoting tube formation, migration, and proliferation of endothelial cells (Fig. 5a).

Moreover, under inflammatory stress, the combined treatment mitigates cellular oxidative stress, decreases the cellular NAD/NADH ratio, and prevents the loss of mitochondrial membrane potential (MMP), thus averting cellular apoptosis (Fig. 5a).

The choice of energy parameters for PBM therapy is critical to its efficacy, and the application of optical doses with low energy density frequently leads to diminished therapeutic efficacy, while excessively high energies may lead to undesirable therapeutic effects^{49,51}. To ascertain the ideal energy density, we conducted energy gradient experiments. The rLED irradiation at $3\text{ J}/\text{cm}^2$ (rLED-M) enhanced CIV activity and ATP production, while the effectiveness significantly decreased as the power density at $5\text{ J}/\text{cm}^2$ (rLED-H), indicating that $3\text{ J}/\text{cm}^2$ is an optimal power density for PBM (Supplementary Fig. 14). Moreover, the F-gel is able to effectively replenish the cellular NAD(H) pool and increase ATP production in HUVECs, while the activity of CIV is not significantly changed (Fig. 5b). The rLED-M together with F-gel significantly restored the cellular NAD(H) reservoir, enhanced the enzymatic activity of CIV in MRC, increased NAD^+/NADH and ATP production, indicating the superior synergy between r&bLED patch and F-gel on mitochondrial function of HUVECs, irrespective of the presence or absence of LPS (Fig. 5b and Supplementary Fig. 15).

To further confirm the synergy between rLED-M and F-gel, we perform EdU proliferation assay and wound scratch assay after different treatments (Fig. 5c,d and Supplementary Fig. 16a, b). The EdU⁺ cell ratio and wound healing rate in the rLED-M combined with F-gel group were notably the highest among all the groups, indicating enhanced cell proliferation and migration (Fig. 5f,g). Tube formation assay is an important method for studying angiogenesis in vitro⁵². As shown in Fig. 5e,h and Supplementary Fig. 16c, the capillary length significantly increased with the combinatory treatment, indicating enhanced tube-forming ability.

Inflammation and the subsequent oxidative stress can trigger a specialized metabolic state that rapidly exhausts intracellular NAD(H), a vital coenzyme essential for numerous energy-producing pathways within the cell, including glycolysis and oxidative phosphorylation⁵³. Therefore, maintaining NAD(H) homeostasis is vital to prevent energy depletion and subsequent cell damage during inflammation. As shown in Fig. 5b, cellular NAD(H) level and CIV activity decline sharply when exposed to LPS, leading to oxidative stress (Fig. 5i,j) and MMP ($\Delta\Psi\text{M}$) decline (Fig. 5k,l and Supplementary Fig. 17), indicating mitochondrial dysfunction in HUVECs. The combination therapy prevented depletion of the cellular NAD(H)-pool and energy and $\Delta\Psi\text{M}$ decrease under LPS stimulation, demonstrating its protective effect on HUVECs in inflammatory situations (Fig. 5i–l).

To investigate the effect of the combination on inflammation regulation in HUVECs, the activation of NF- κB p65 was observed using confocal laser scanning microscopy (CLSM) (Fig. 5m and Supplementary Fig. 18). P65 nuclear translocation induced by LPS was significantly reduced by rLED-M combined with F-gel treatment, with increased efficacies of the combined therapy (Fig. 5n). Improved mitochondrial function is likely to prevent apoptosis, which is a common response of endothelial cells to inflammation⁵⁴. As shown in Fig. 5o–r, the combination therapy effectively suppressed cell damage and apoptosis induced by the inflammatory factors of LPS (Fig. 5o,p) and TNF- α (Fig. 5q,r), demonstrating its therapeutic efficacy extends to various inflammatory mediators. The above results showed that the combination of r&bLED and F-gel could synergistically promote tube formation, cell proliferation, migration, and prevent inflammation-induced apoptosis through improving ETC and MRC in HUVECs, suggesting a positive role in accelerating angiogenesis in infected wound.

r&bLED patch combined with F-gel regulates macrophage polarization through energy-based metabolic reprogramming

Monocyte/macrophage lineage (MΦs) play a crucial role in the innate capacity of the body to rejuvenate tissue function following injury⁵⁵.

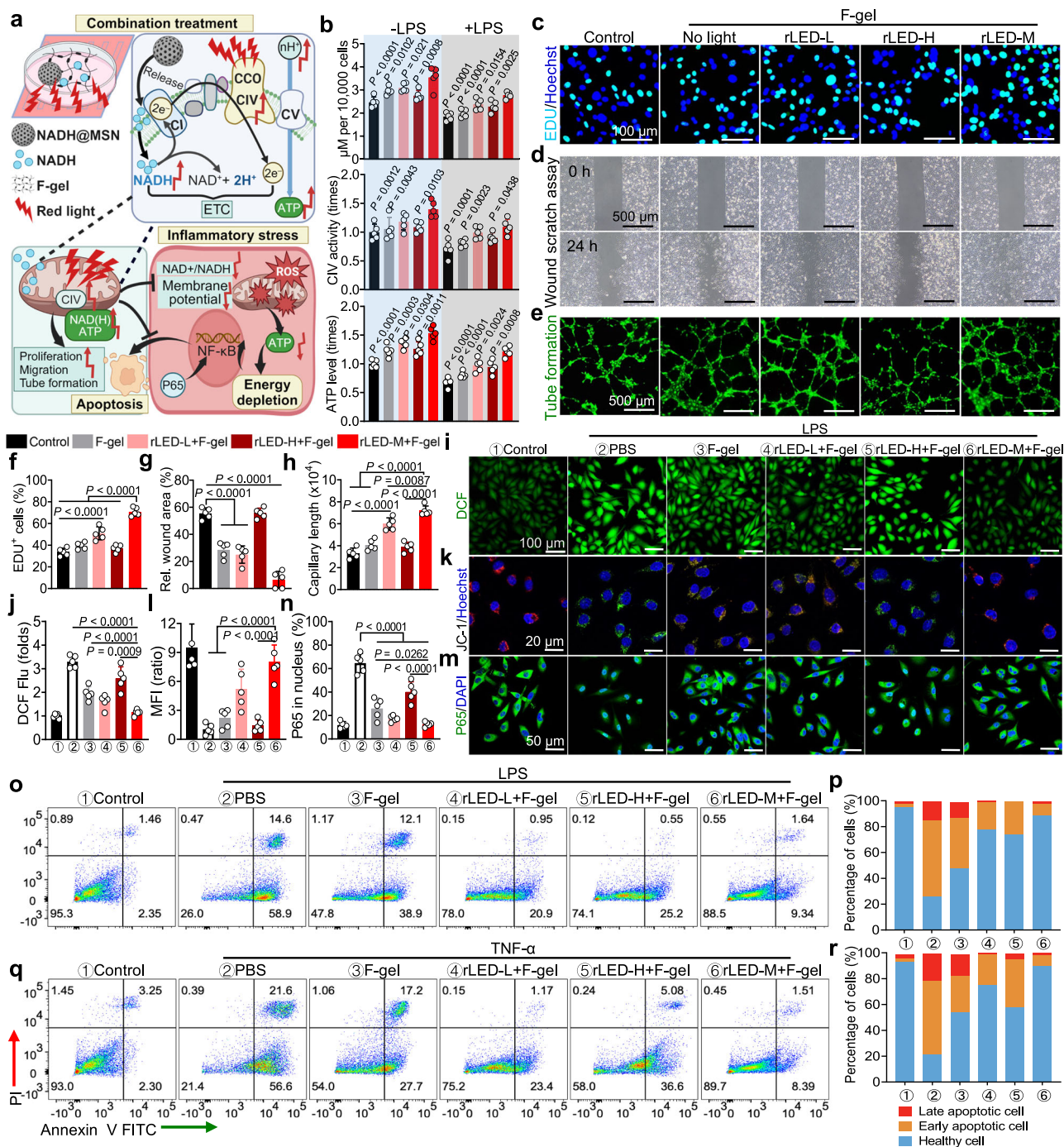


Fig. 5 | r&bLED together with F-gel synergistically accelerates angiogenesis via improving MRC. **a** Schematic diagram of the mechanisms of rLED combined with F-gel to improve mitochondrial function. **b** Intracellular NAD(H) levels, CIV activity and ATP level in HUVECs after cocultured with or without LPS, F-gel (NADH concentration, 100 μ M) and rLED with different energy densities (rLED-L, 1 J/cm²; rLED-M, 3 J/cm²; rLED-H, 5 J/cm²). **c, f** Representative EdU staining micrographs (c) and statistical analysis (c) of positive ratios of HUVECs with different treatments for 24 hours. **d, g** Wound scratch assay of HUVECs observed by an optical microscope (d) and the calculation of relative wound area (g). **e, h** Tube formation of HUVECs (e) and the Statistical analysis of capillary length (h) after treatment. **i, k, m** Intracellular ROS (i), mitochondrial membrane potential ($\Delta\Psi$ M) (k) and NF- κ B p65 nuclear

translocation (m) of HUVECs observed by CLSM after cocultured with or without LPS and different treatments. **j, l, n** Statistical analysis of intracellular ROS (j), mitochondrial membrane potential ($\Delta\Psi$ M) (l) and NF- κ B p65 nuclear translocation (n) of HUVECs. **o, q** HUVECs apoptosis triggered by LPS (100 ng/mL, 48 h) and TNF- α (80 ng/mL, 48 h) analyzed by Annexin V/PI double staining. **p, r** Quantitative analysis of LPS (p) and TNF- α (r) triggered apoptosis in HUVECs. Values in b, f-h, j, l, n represent the mean \pm s.d. (n = 5 biologically independent samples in each group). Data are presented as mean values \pm SEM. Statistical significance and P values were determined by one-way ANOVA followed by Tukey's multiple comparison test. Panel a was created with BioRender.com released under a Creative Commons Attribution-NonCommercial-NoDerivs 4.0 International license.

Previous research has demonstrated that M Φ s swiftly transition through various activation states in response to the damaged tissue microenvironment for an effective wound healing⁵⁶. NADH loaded in F-gel and rLED were employed to regulate macrophage polarization.

NAD(H) is known as an immunomodulator and can downregulate the production of inflammatory factors through sufficient energy supplement^{9,57}. Meanwhile, PBM counteracts the inhibitory effects of NO on the CIV binding site, which is a rate-limiting step in MRC,

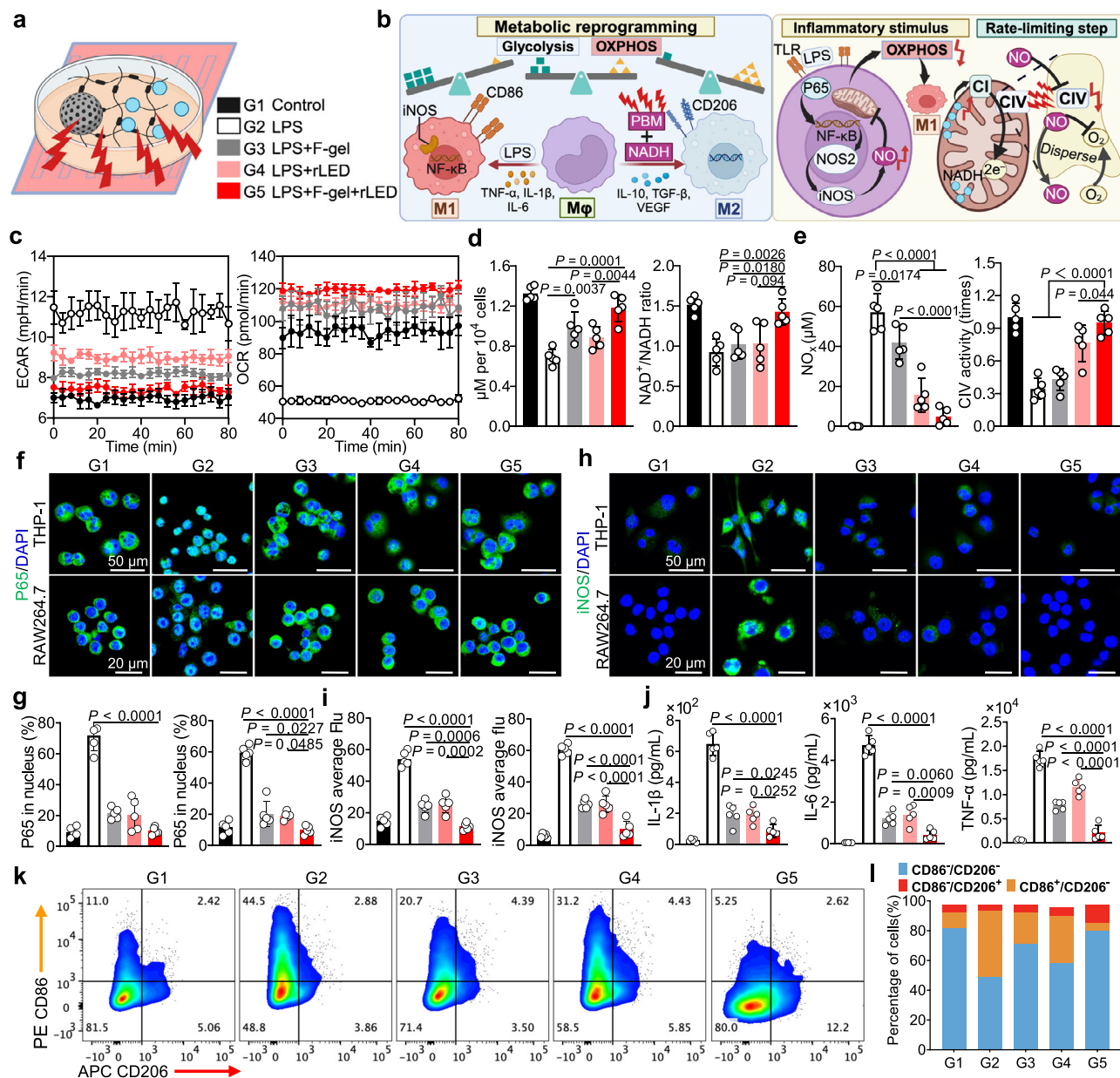


Fig. 6 | r&bLED patch combined with F-gel regulate macrophage polarization through energy-based metabolic reprogramming. **a** Schematic diagram of the protocol (G1, Control; G2, LPS; G3, LPS + F-gel; G4, LPS + rLED; G5, LPS + F-gel + rLED) (rLED, 3 J/cm²; NADH concentration in F-gel, 100 μM). **b** Schematic diagram of the mechanisms of rLED combined with F-gel to regulate macrophage polarization through metabolic reprogramming. **c** Real-time measurement of ECAR and OCR (c) of THP-1 cells left unstimulated (control) or stimulated with LPS. **d** Intracellular NAD(H) levels (left) and NAD⁺/NAD(H) ratio (right) in THP-1 cells after different treatment. **e** Intracellular NO_x levels (left) and CIV activity (right) in THP-1 cells after different treatments. **f, g** NF-κB p65 nuclear translocation of THP-1 and RAW264.7 cells observed by CLSM (f) after cocultured with or without LPS and different

treatments and quantitative analysis of P65 intensity in the nucleus (g). **h, i** iNOS of THP-1 and RAW264.7 cells observed by CLSM (h) after different treatments and quantitative analysis of average fluorescence intensity (i). **j** Pro-inflammatory cytokine levels in THP-1 cells culture supernatant quantified by ELISA. **k** Flow cytometry analysis of CD206 and CD86 expression in THP-1 cells. **l** Quantitative analysis of CD86⁺/CD206⁺, CD86⁺/CD206⁻ and CD86⁻/CD206⁺ cells. Values in c-e, g, i, j represent the mean ± s.d. (n = 5 biologically independent samples in each group). Statistical significance was calculated via one-way ANOVA followed by Tukey's multiple comparison test. Panel a and b was created with BioRender.com released under a Creative Commons Attribution-NonCommercial-NoDerivs 4.0 International license.

resulting in enhanced OXPHOS and improved mitochondrial function⁴⁹. Therefore, the combination may regulate macrophage polarization through energy-based metabolic reprogramming (Fig. 6a,b).

The Extracellular Acidification Rate (ECAR, a measure of lactate production that reflects glycolysis rate) and Oxygen Consumption Rate (OCR, a readout of oxidative phosphorylation) serve as main indicators reflecting macrophage metabolism^{53,56}. ECAR increased sharply, when THP-1 cells were incubated with LPS (100 ng/mL)

without additional treatment, indicating the burst of glycolysis; nevertheless, pre-irradiation of cells with rLED or application of F-gel 2 hrs prior to LPS incubation did not show a significant rise in ECAR like G2 group, and the combined treatment exhibited the most favorable outcome, bringing down ECAR levels nearly to those of the Control (G1 group) (Fig. 6c, left). Similarly, the OCR in G2 decreased drastically after incubation with LPS, indicating the reduction of OXPHOS, while the combinatory treatment enhanced OXPHOS and prevented mitochondrial dysfunction, restoring OCR to normal or higher levels

(Fig. 6c, right). To further investigate the impact of combined treatment on the mitochondrial function of macrophage, cellular NAD(H) and NAD⁺/NADH ratios were analyzed. As shown in Fig. 6d, F-gel significantly prevented the cellular NAD(H) reservoir depletion resulting from LPS stimulation, while the combined treatment showed a better outcome (left). Similarly, the combinatory treatment increased the NAD⁺/NADH ratio, indicating improved cellular redox status (right). Furthermore, the content of NO, which can inhibit CIV activity in ETC, showed that rLED together with F-gel significantly inhibited NO generation (Fig. 6e, left) and enhanced the CIV activity (Fig. 6e, right). These results demonstrated the combination treatment may achieve energy-based metabolic reprogramming in macrophages.

To further investigate the effect of the combination on inflammation gene transcription, NF- κ B p65 nuclear translocation (Fig. 6f,g and Supplementary Fig. 19) and the expression of iNOS (Fig. 6h,i and Supplementary Fig. 20) were observed by CLSM in THP-1 (up) and RAW264.7 (down) cells. As shown in Fig. 6f and g, p65 nuclear translocation induced by LPS was significantly decreased by rLED together with F-gel treatment in two cell lines. Moreover, the expression of iNOS, which is a marker of M1 macrophage⁵⁸, was significantly reduced by the combination treatment (Fig. 6h,i), evidenced by drastic decreases in the expression of inflammatory factors, including IL-1 β , IL-6 and TNF- α in THP-1 (Fig. 6j) and RAW264.7 cells (Supplementary Fig. 21). The anti-inflammatory effects were further validated by flow cytometry detection of CD206 and CD86 in THP-1 (Fig. 6k,l) and RAW264.7 (Supplementary Fig. 22) cells. These results demonstrated that the combination therapy modulated macrophage repolarization into M2 phenotype and suppressed inflammation via energy metabolism-immune regulatory pathway, in favor of the healing of chronic wounds.

In vivo efficacy on enhancing healing of infected diabetic wound in mice

Encouraged by the angiogenesis and inflammation regulation induced by the combination treatment in vitro, we investigated the therapeutic effects in infected diabetic mouse wounds. The treatment strategy is illustrated in Fig. 7a, including STZ *i.p.* injection, wounding, and *lux* MRSA or *Pa* inoculation in BALB/c mice, followed by the various treatments. The infected diabetic mice were randomly divided into five groups: G1, control; G2, F-gel; G3, rLED+F-gel; G4, bLED+F-gel; G5, r&bLED+F-gel. Bioluminescent MRSA and *Pa* were used for real-time tracking of skin infection progression using IVIS. The bioluminescent MRSA strain derived from ATCC 33591, and the bioluminescent *Pa* was genetically modified with the *lux* pGEX-Apr operon to emit bioluminescence, operon expression and linear correlations ($R^2 = 0.9800$) between bioluminescence intensity and CFU were verified prior to the test (Supplementary Fig. 23). Following the development of wound infection on the second day, the wounds were treated according to their respective groups (Fig. 7b and Supplementary Fig. 24a). Bacterial luminescence of the wound decreased in a bLED dose-dependent manner, and bLED exposure for 12 min (36 J/cm²) completely eliminated 8.3 lg luminescence in MRSA and 8.0 lg luminescence in *Pa*, whereas F-gel or F-gel with rLED did not significantly reduce luminescence (Fig. 7b,c and Supplementary Fig. 24a,b). The bactericidal activity was further confirmed at the end of experiments by observing corresponding CFU reduction within the infected wounds (Fig. 7b). Moreover, we failed to detect any viable bacteria in the wounds 12 days after the combined treatment, meaning that r&bLED and F-gel synergistically cured the acute MRSA infection completely (Fig. 7d).

To assess wound healing efficacy, the MRSA- and *Pa*-infected wounds were monitored over time. At days 8, 12, and 16, mice in G5 displayed the most significant wound healing progress, with minimal visible scars compared to the other groups. In contrast, distinct scars were still present in the control group (Fig. 7e and Supplementary Fig. 24c). The wound healing rate curve further corroborated aster

wound healing in the G5 group, with nearly complete closure, than other groups, particularly when compared with the control group (Fig. 7f and Supplementary Fig. 24d), suggesting combination therapy effectively promoted healing of infected diabetic wounds.

The formation of granulation tissue is crucial for effective wound healing. Histological examination with H&E staining demonstrated a substantial increase in the thickness of granulation tissue following combination therapy, as compared to the control group (Fig. 7g,h and Supplementary Fig. 24e,f). Moreover, G5 exhibited elevated collagen deposition compared to other groups on both day 8 and day 16 (Fig. 7i, j and Supplementary Fig. 24g,h), suggesting superior wound healing quality. To investigate the impact of combination treatment on in vivo angiogenesis, histological analysis was conducted using immunofluorescence staining of CD31 and α -SMA. A notably higher number of vessels were observed in G5 on day 8 compared to other groups (Fig. 7k,l). These findings suggest that the combination treatment effectively enhances neovascularization and expedites wound healing. Furthermore, the number of wound vessels decreased on day 16 compared to day 8, potentially indicating the transition from the proliferative phase to the remodeling phase per the typical angiogenesis pattern during wound healing⁵⁹.

To further elucidate the mechanism associated with mitochondrial functions underlying the enhancement of wound healing by combination therapy, the NAD⁺/NADH ratio, CIV activity and ATP productions in wound tissues were evaluated. On both days 8 and 16, the NAD⁺/NADH ratio in G5 was significantly higher than in other groups, with a similar trend observed in CIV activity (Fig. 7m,n), indicating an enhancement in mitochondrial function within the wound tissue due to the combination therapy. Enhancements in mitochondrial function were further validated through the assessment of ATP levels within the tissue, demonstrating the combination treatment enhanced healing of MRSA-infected diabetic wounds via energy supplement (Fig. 7o).

Effects of r&bLED patch combined with F-gel for inflammatory regulation in vivo

Wound healing is a well-coordinated process that advances through distinct phases, including hemostasis, inflammation, proliferation, and remodeling. However, this process is disrupted in diabetic wounds, characterized by prolonged low-grade inflammation, which could be typically characterized by predominant M1 macrophages and pro-inflammatory cytokines including IL-6 and TNF- α , hindering the progression of wound healing⁶⁰. In accordance with excessive inflammation in the wound, the secretion of pro-inflammatory TNF- α and IL-6 was high in the control wound, which was significantly down-regulated in G3 and G5, whereas the decrease in G2 was not significant, indicating the superior anti-inflammatory effect of combination treatment (Fig. 8a and Supplementary Fig. 25a,b). In addition to pro-inflammatory cytokines, the phenotype of macrophages recruited to the injury site is also a crucial indicator of the inflammatory response^{8,61}. CD86 and CD206 were selected as typical surface markers for M1 or M2 macrophages, respectively. As shown in Fig. 8b and Supplementary Fig. 25c,d, r&bLED together with F-gel notably elevated the presence of M2 macrophages (CD206⁺) with a superior effect observed on both days 8 and 16, in comparison with other groups. Conversely, the combined treatment reduced the ratio of M1 macrophages (CD86⁺) on days 8 and 16.

To further evaluate the attenuation of chronic inflammation following combination therapy, transcriptome analysis of the wound tissue was conducted on day 8, overlaying both the inflammatory and proliferative phases. Differentially expressed 376 genes were identified between G1 and G5 (fold change ≥ 2 and $q < 0.05$) (Fig. 8c). GO enrichment analysis illustrated decreases in genes related to inflammatory responses (like *CCL7*, *CCR1*, *CD14*, *CXCL1*, *CXCL3*, *CXCL5*, *Elf3*, *Fpr1*, *IL18rap*), innate immune response (like *Cd14*, *Cfi*, *Clec4e*, *Ifitm1*,

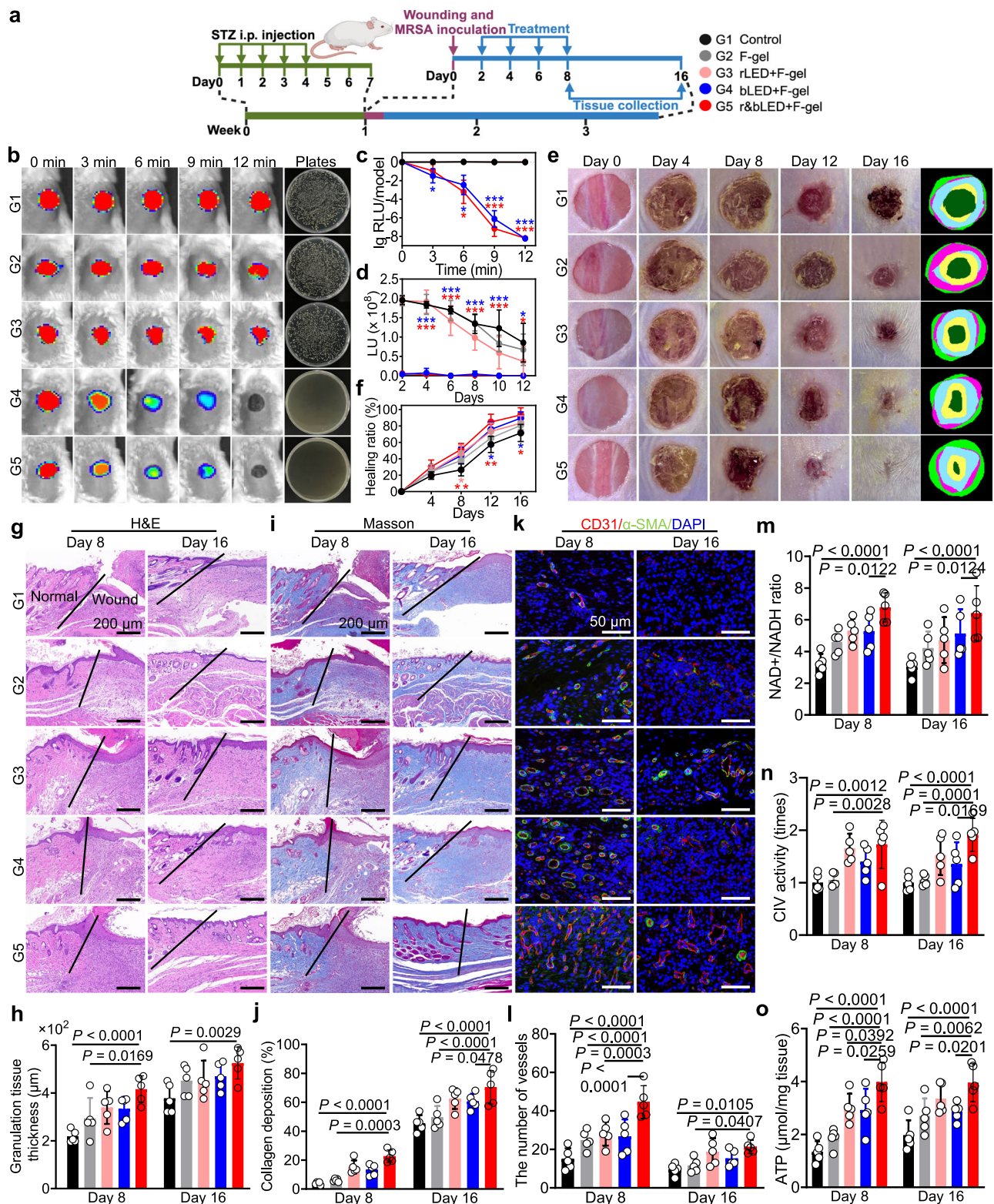


Fig. 7 | In vivo efficacy on enhancing healing of MRSA-infected diabetic wound mouse model. **a** The study protocol including STZ *i.p.* injection, wounding and MRSA inoculation in BALB/c mice, followed by the treatments (G1, control; G2, F-gel; G3, rLED+F-gel; G4, bLED+F-gel; G5, r&bLED+F-gel) (rLED, 3 J/cm²; bLED, 36 J/cm²; NADH concentration in F-gel, 100 μ M; TQ concentration in F-gel, 200 μ g/mL). **b** Bacterial luminescence images of acutely infected wounds and representative photographs of microbacterial agar plates. **c** Mean luminescence was expressed as logarithmic relative luminescence units (lg RLU) per model relative to time zero. **d** Bacterial burdens in the wounds were evaluated after bacterial inoculation. **e** Representative photographs of skin wounds. **f** Quantitative data of wound healing ratio within 16 days of the different

groups at different time points. **g, i, k** Representative images from day 8 and day 16 wounds with H&E (**g**), MTS (**i**), and immunofluorescence staining for CD31 and α SMA (**k**). **h, j, l**, Quantification of the granulation tissue thickness (**h**), collagen deposition ratio (**j**) and number of vessels (**l**) in different groups on day 8 and day 16. **m-o**, NAD⁺/NAD(H) ratio (**m**), CIV activity (**n**) and ATP level (**o**) in wound tissue after different treatments. Values in **c, d, f, h, j, l, m-o** represent the mean \pm s.d. ($n = 5$ biologically independent samples in each group). Data are presented as mean values \pm SEM. Statistical significance was calculated via two-way ANOVA followed by Dunnett's multiple comparison test. Panel **a** was created with BioRender.com released under a Creative Commons Attribution-NonCommercial-NoDerivs 4.0 International license.

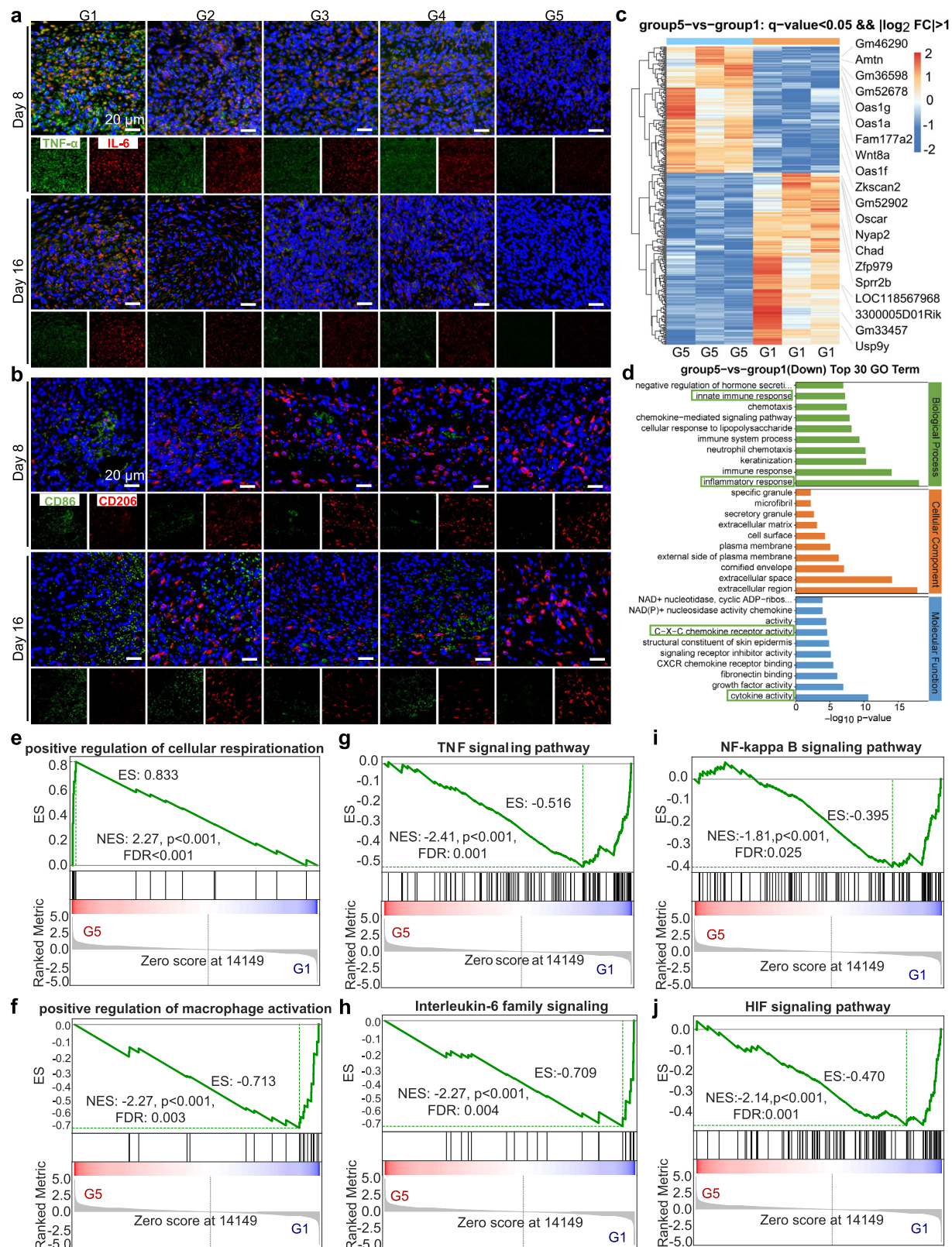
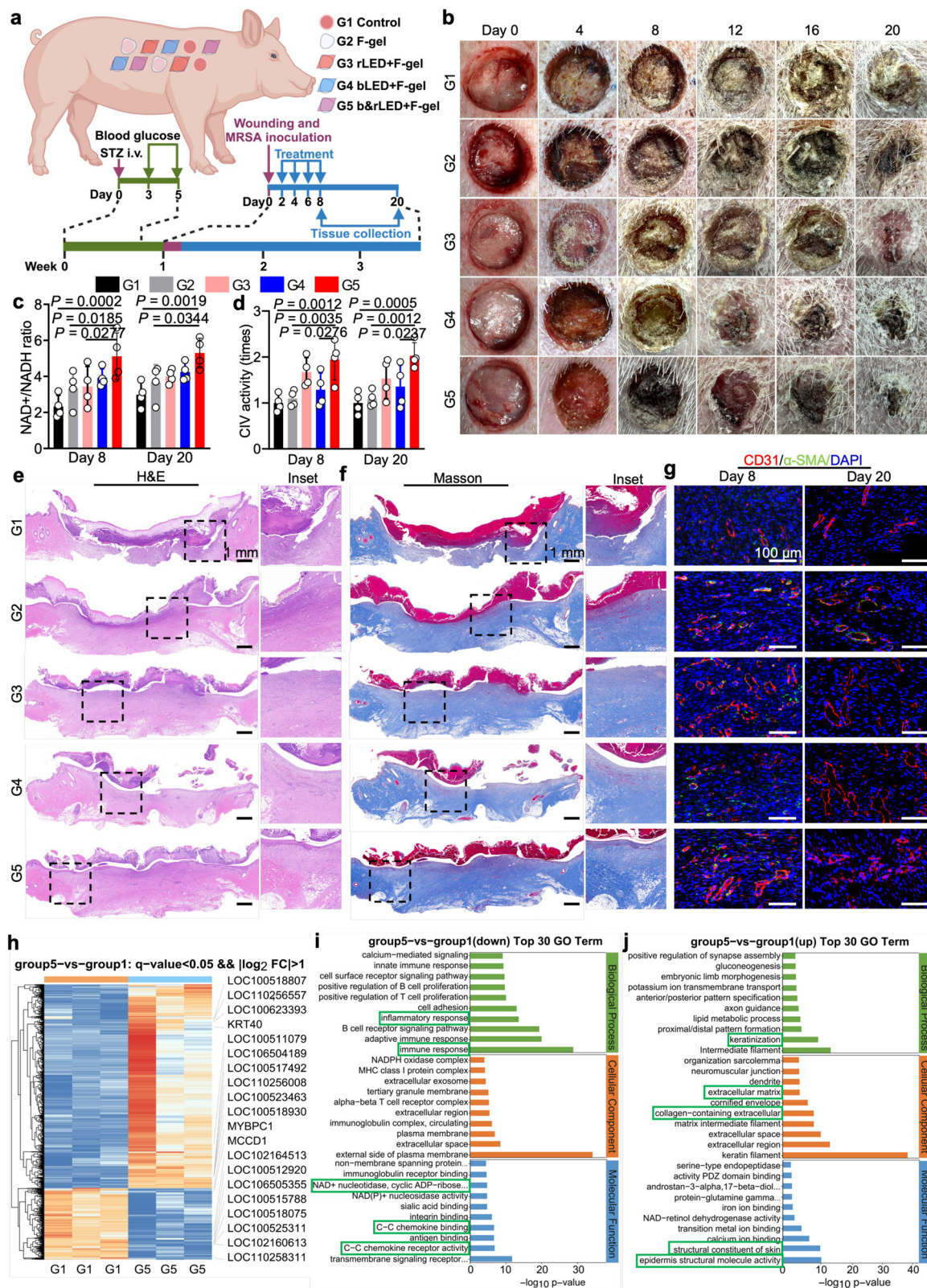


Fig. 8 | Effects of r&bLED patch combined with F-gel for inflammatory regulation in vivo. a, b Representative images from day 8 and day 16 wounds with immunofluorescence staining for IL-6/TNF α (a) and CD86/CD206 (b). **c** Heat map and

functional classification of the differentially expressed genes of wound tissue after treated with PBS or F-gel with r&bLED (fold change ≥ 2 and $q < 0.05$). **d** GO enrichment analysis of the down-regulated genes. **e-j** Gene Set Enrichment Analysis (GSEA) image.

Krt16, *Mefv*, *Nlrp3*, *Oas3*, *Rarres2*), cytokine activity (like *IL11*, *IL1rn*, *IL24*, *IL6*, *Inhba*, *Lif*, *Osm*, *Spp1*, *Timp1*) and C-X-C chemokine receptor activity (like *CXCR1*, *CXCR2*, *Gpr35*), which are mainly related to inflammation, confirming the anti-inflammatory effect of combinatory

therapy (green rectangle) at molecular levels (Fig. 8d). Excitingly, genes associated with the positive regulation of cellular respiration (like *Oas1a*, *Oas1e*, *Oas1f*, *Oas1g*) were enriched in both GO analysis and GSEA (Fig. 8e and Supplementary Fig. 26a,b), providing further



evidence of the enhancement of mitochondrial functions within the tissue. In addition, GSEA showed down-regulation in genes related to activation of macrophage (like *Wnt5a*, *Cebpa*, *Il10*, *Pla2g4a*, *Kars*, *Lgals9*) (Fig. 8f and Supplementary Fig. 26c). Moreover, the GSEA and KEGG enrichment revealed decreased expressions of TNF- α (like *IL1b*, *Map3k14*, *CXCL3*, *Ptgs2*, *Map2k1*, *Nfkb1a*, *Nod2*, *Casp3*), IL-6 (like *IL6*, *Crlf1*, *Osm*, *CLCF1*, *Lif*, *IL11*, *Socs3*) and NF- κ b signaling pathway (like

Cd14, *Cxcl1*, *Cxcl3*, *Nfkb1a*, *Ptgs2*, *Tnfsf11*, *Tnfsf14*) (Fig. 8g-i and Supplementary Fig. 26d), consistent with the findings from histological testing and biochemical analysis. Notably, activation of the HIF signaling pathway is indicative of tissue hypoxia⁶², and GSEA revealed a downregulation of the HIF signaling pathway (like *NOS2*, *NOS3*, *Hmox1*, *Map2k1*, *Pgk1*, *Hk2*, *HIF1a*), suggesting improved vascularization following combined treatment (Fig. 8j). These findings indicate that

Fig. 9 | r&bLED together with F-gel enhances wound healing in the infected diabetic minipig. **a** The study protocol including STZ *i.v.* injection, blood glucose monitoring, wounding and MRSA inoculation in panama minipigs, followed by the treatments (G1, control; G2, F-gel; G3, rLED+F-gel; G4, bLED+F-gel; G5, r&bLED+F-gel) (rLED, 3J/cm²; bLED, 36J/cm²; NADH concentration in F-gel, 100 μM; TQ concentration in F-gel, 200 μg/mL). **b**, Representative photographs of porcine wounds. **c**, **d** NAD⁺/NAD(H) ratio (**c**) and CIV activity (**d**) level in wound tissue after different treatments (*n* = 5 biologically independent samples in each group, data are presented as mean values ± SEM, statistical significance was calculated via two-way

ANOVA followed by Dunnett's multiple comparison test). **e**, **f** Representative images from day 8 wounds with H&E (**e**) and MTS staining (**f**). **g** Representative images from day 8 and day 20 wounds with immunofluorescence staining for CD31 and αSMA. **h** Heat map and functional classification of the differentially expressed genes of wound tissue in G1 and G5 (fold change ≥ 2 and *q* < 0.05). **i**, **j** GO enrichment analysis of the down-regulated (**i**) and up-regulated (**j**) genes. Panel **a** was created with BioRender.com released under a Creative Commons Attribution-NonCommercial-NoDerivs 4.0 International license.

combined therapy effectively dampened inflammation and enhanced wound healing via energy metabolism-immune pathway *in vivo*.

r&bLED together with F-gel enhances wound healing in the infected diabetic minipig

To further validate the efficacy of the combination therapy, we employed a porcine wound healing model that closely resembles the human wound healing process. Porcine skin shares many similarities with human skin, including comparable dermal and epidermal architecture, substantial subcutaneous adipose depots, sparse distribution of hair follicles, and the presence of structures such as rete ridges⁶³. STZ was injected *i.v.* into Panama minipigs to induce diabetes. After monitoring blood glucose for one week to confirm diabetes status, a series of circular and full-thickness wounds 1.5 cm in diameter were created on both sides of the porcine back (Fig. 9a). Subsequently, 100 μL of MRSA suspension at a concentration of 1×10^9 CFU/mL was applied onto each wound to induce acute skin infection. The infected wounds were then divided into five groups randomly. Following the development of wound infection on the second day, the wound was subjected to different treatments, and the therapies were administered every 2 days until day 8.

On day 2 after treatment, CFU counts of MRSA colonies from wound exudate demonstrated the excellent antibacterial effect of bLED combined with F-gel (Supplementary Fig. 27a). In addition, Wounds in G1, G2, and G3 exhibited purulent exudates on day 4 and delayed scab formation, consistent with infections (Fig. 9b). Meanwhile, wounds in G4 and G5 were dry and showed accelerated scab formation, indicating a faster healing process with the help of bLED irradiation and F-gel. In addition, the granulation tissue exhibited accelerated growth, epithelialization progressed rapidly and scab detachment occurred effortlessly in G5, leading to an earlier attainment of complete wound healing. Conversely, within the G1 group, epithelial migration was slow, and the scab adhered tightly, impeding its natural detachment (Fig. 9b). To further demonstrate the improvement of mitochondrial function after combination treatment, the NAD⁺/NADH ratio and CIV activity were assessed in porcine wound tissue. On days 8 and 20, the NAD⁺/NADH ratio and CIV activity were significantly higher in the G5 group than in the other groups, suggesting an improvement in mitochondrial function within the wound tissue attributed to the combination therapy (Fig. 9c,d). Moreover, the F-gel and r&bLED-treated wounds demonstrated expedited wound closure, the lowest open wound and the thickest granulation tissue thickness at both examined time points (Fig. 9e, Supplementary Fig. 27b-d). On days 8 and 20, the wounds in G5 had increased re-epithelialization, and by day 20, all wounds were almost fully re-epithelialized (Fig. 9e and Supplementary Fig. 27b). In addition, G5 exhibited elevated collagen deposition ratios compared to other groups on both days 8 and 20 (Fig. 9f and Supplementary Fig. 28). Enhanced immunostaining for CD31 and α-SMA suggested angiogenesis promoted by the combination treatment on days 8 and 20, which was significantly different from G1 and G2 on day 8 (Fig. 9g and Supplementary Fig. 29).

To further investigate the mechanism underlying the enhanced wound healing facilitated by the combination therapy in the infected

porcine wound model, transcriptome analysis of wound tissue was performed on day 8. Differentially expressed 1754 genes were identified between G1 and G5 (fold change ≥ 2 and *q* < 0.05) (Fig. 9h). GO enrichment analysis revealed down-regulation in genes related to inflammation, including inflammatory response (like *ACOD1*, *ADAM8*, *AMCF-II*, *C5AR1*, *CCL19*, *CCL2*, *CCL20*), C-C chemokine receptor activity (like *ACKR3*, *CCR1*, *CCR2*, *CCR6*, *CCR7*, *CXCR4*), NAD⁺ nucleotidase (like *BST1*, *CD38*, *IL18RAP*, *TLR10*, *TLR2*) and C-C chemokine binding (like *ACKR3*, *CCR1*, *CCR2*, *CCR6*, *CCR7*), reaffirming the anti-inflammatory effect of combinatory therapy (green rectangle) at molecular levels (Fig. 9i). In addition, genes associated with tissue repair were up-regulated, including keratinization (like *KRT1*, *KRT2*, *KRT3*, *KRT5*, *KRT74*, *KRT77*, *KRT79*), extracellular matrix (like *ACAN*, *ADAMTS18*, *ADAMTS8*, *ANOS1-2*, *CCBE1*) and structural constituent of skin epidermis (like *KRT77*, *KRT79*, *KRT82*, *KRT84*, *LOC100511079*, *LOC1005240*) (green rectangle) (Fig. 9j), providing further evidence of the enhancement for wound healing after the combined treatment. Furthermore, GSEA enrichment showed down-regulation in genes related to inflammation and up-regulation in genes related to tissue repair, consistent with the findings from GO enrichment (Supplementary Fig. 30a-f). These findings in minipigs provide convincing evidence that the combination treatment effectively combats microbial infection and facilitates diabetic wound healing through modulation of the energy metabolism-immune pathway.

Discussion

Non-healing chronic wounds significantly diminish the quality of life for affected individuals and strain healthcare systems, which have been identified by the FDA as a top priority of the research area⁶⁴. The morbidity and associated costs of chronic wounds, including severe outcomes like amputation and death, persistently rise, with a 5-year mortality rate similar to cancer⁶⁵. However, unlike diseases such as cancers, where treatment strategies are well-established, addressing chronic wounds is still a “trial and error” approach that remains a costly and ineffective process due to their diverse causes, including infections by various pathogens, biofilms, and pro-inflammatory bacterial toxins. These factors, combined with the heterogeneous nature of wounds among patients, contribute to treatment challenges and the progression of wounds to advanced stages despite standard care. Despite numerous clinical trials, meaningful improvements in outcomes have remained elusive. Over the past 26 years, only one FDA-approved pharmacological agent for chronic wounds, Becaplermin, has emerged, despite its associated cancer risk and safety warning label^{64,66}. The management of chronic wound encompasses various interventions, such as debridement, employing negative pressure wound therapy, applying growth factors externally, and utilizing skin substitutes for coverage, among other methods⁶⁷. Conventional approaches are often associated with long treatment times, sub-optimal outcomes and significant costs, demanding for new approaches to effective and cost-effective chronic wound management, particularly for low-income populations.

Many studies have explored the use of light for PDT and PBM to eradicate microbial infections and facilitate wound healing, with fewer side effects on healthy tissue^{31,68,69}. However, conventional

phototherapy devices are associated with high treatment costs and offer limited comfort during treatment, requiring frequent hospital visits, limiting the effectiveness and broad adoption for phototherapy (Supplementary Table 2). To address these issues, we developed a wearable and stretchable dual wavelength r&bLED patch for home phototherapy, using simple manufacturing processes and low-cost materials for large-scale personalised production. The patch exhibits as a comfortable wearable device, which is paper-thin, flexible, and stretchable, sticks nicely to the skin, and may be used while exercising. In addition, this patch is well-suited for phototherapy applications as it offers adjustable light power density, uniform light distribution, and eliminates any areas of insufficient light coverage. Moreover, the patch treatment ensures exceptional safety features, including low lamp bead driving voltage, minimal heat generation, real-time monitoring of therapeutic area temperature, biocompatible PDMS materials, protective packaging for the tissue fluid circuit, and temperature alarms to provide additional safety measures (Supplementary Table 2). In addition, patients can conveniently control the switch and power of the light using the mobile app and concurrently monitor the real-time temperature of the treatment area, making the wearable LED patch user-friendly and effortlessly to operate, which is well-suited for phototherapy applications at home for chronic wound, including but not limited to wound in aging populations, diabetic ulcers, pressure ulcers, venous ulcer, burn wounds. To enhance the therapeutic efficacy of r&bLED patch while minimizing damage to normal tissue, we developed a sprayable and in-situ formed F-gel by co-loading with blue light-sensitive TQ and red light-synergistic NADH. The LED patch and F-gel synergistically combat microbial infections and facilitate wound healing (Fig. 3). The combination treatment is cost effective as there are no skilled technicians or doctors involved. Moving forward, as next-generation stretchable LED technology advances and becomes industrialized, we will further explore its application in phototherapy devices.

Chronic wounds serve as a favorable environment for pathogenic microorganisms to thrive. These microbes secrete toxic enzymes that can harm host tissue and interfere with the wound healing process, resulting in heightened inflammation, delayed wound healing and may result in serious complications⁷⁰. Infectious wounds necessitate frequent hospital visits for treatment, imposing significant financial and psychological strains on patients. Worse still, the overuse, misuse, and abuse of antibiotics frequently lead to the escalation of microbial resistance, resulting in a sharp increase in treatment cost, duration and patient mortality rate^{6,7}. PDT, a minimally invasive procedure that does not raise concerns of drug resistance, has received widespread attention as an antibacterial method^{71,72}. The LED patch irradiation and F-gel can produce ROS, including $\cdot\text{OH}$, H_2O_2 and $\text{O}_2\cdot^-$, under bLED irradiation, as confirmed by fluorescent probe and EPR. The combination of bLED irradiation and F-gel demonstrated the ability to eliminate a variety of microbes, including multi-drug resistant MRSA, *Pa*, *Ab* and the common clinical fungal infection *Ca* (Fig. 4a). In addition, the presence of NADH loaded in F-gel reduces the ROS-induced damage caused by PDT to healthy tissues. The combination therapy provides a practical, cost-effective, and convenient home treatment option for infected wounds.

Wound healing is a highly metabolically demanding process and mitochondrial dysfunction is closely linked to the development of chronic wounds that are characterized by prolonged inflammation and impaired vascularization^{73–77}. PBM stimulates CIV, a key rate-limiting enzyme in the cellular respiratory chain, increases the flux through the ETC, and improves mitochondrial function⁷⁸. NADH is a vital hydrogen donor for the ETC and serves as a key substrate within the MRC. Our study showed that the combination of PBM with NADH-loaded F-gel synergistically improved mitochondrial function in HUVECs under inflammatory stress, resulting in synergistical promotion of wound vascularization via energy supplement (Fig. 5a). Moreover, the combination therapy improved mitochondrial function in macrophages

under LPS stimulation, leading to the enhancement of OXPHOS. The combination treatment induces metabolic reprogramming of macrophages, directing them toward the anti-inflammatory M2 phenotype via the energy metabolism-immune regulatory pathway (Fig. 6b).

The antimicrobial, pro-angiogenic, and anti-inflammatory effects of the combination treatment are further demonstrated through experiments conducted on an infected diabetic wound model in mice and minipigs. In summary, the data from preclinical diabetic wound healing models corroborate our hypothesis, indicating that r&bLED patches combined with F-gel offer a promising therapeutic approach for effectively managing chronic wounds. This treatment modality holds great promise for clinical interventions for chronic diabetic wounds at home, especially if a prototype is developed capable of monitoring infection and healing progress in real-time.

Methods

Reagents and materials

All chemicals were obtained from Sigma-Aldrich unless otherwise mentioned and used without further purification. Antibodies used in this article were listed in Supplementary Table 3.

Fabrication and characterization of r&bLED patches

The TPU substrate was used as the initial substrate and via holes were created to connect the bottom and top layers. Subsequently, the substrate was coated with AgNW on both sides using a multi-functional flexible electronic printing (Shanghai Mifang Electronic Technology Co., Ltd., MF-MP3300, China). The typical size of the TPU substrate was 4 cm × 4 cm and 2 cm × 2 cm, and the thickness of the TPU patterns was set to 20 μm . The packaged rLED chips (wavelength = 630 nm; REFOND, China) and bLED chips (wavelength = 470 nm; REFOND, China) alone with a temperature sensor (MI17Z, Mysentech) were manually placed on the contact pads after applying high-density conductive silver paste (Shanghai Mifang Technology, China), and then a reflow process was performed at a temperature of 90 °C with a melting interval duration of 3 min. PDMS was then applied to the surface mount LEDs using a dip coating process (10:1 mixing ratio of prepolymer and hardener; SYLGARD 184, Dow, USA) and cured overnight in an oven at 70 °C. Finally, the back of the substrate is encapsulated with PDMS mixed with reflective paint to prevent light from escaping from the back.

The optical power density of the r&bLED patch was measured by an optical power meter (PM100D, Thorlabs, USA), and the mechanical durability of the r&bLED patch was repeatedly tested by load pressure in the folded state (Shanghai Mifang Technology, China). The heat generation of the r&bLED patch was measured by thermal infrared image camera (E54, FLIR, Shanghai, China).

Fabrication of control module

The control module comprises a rigid FR4 printed circuit board (PCB), surface-mounted electronic components, a battery, and encapsulation. The two-layer custom PCB was designed using JLCEDA (Professional) and fabricated by an ISO 9001: 2015-certified vendor (JLPCB.com). The device features a 0.4-mm-thick FR4 PCB with a solder mask and electroless nickel immersion gold (ENIG) finish on the exposed pads. Electronic components, including the ESPSoC and peripherals, were affixed to the PCB using a lead-free solder paste (AZ50 Solder Paste, Anrecon). The ESPSoC was programmed with custom embedded firmware developed in Arduino IDE 2.3.2.

The device shell was produced using a DLP light-cured 3D printer (Anycubic Photon D2) and designed with SolidWorks 2019 (Education Edition). The .stl files were prepared for slicing with the Anycubic Slicer, followed by 3D printing and post-processing (Wash and Cure 2.0, Anycubic) with various photosensitive resins.

The assembly of the PCB with the lithium battery was encased within the device shell, followed by encapsulation using PDMS(10:1

mixing ratio of prepolymer and hardener; SYLGARD 184, Dow, USA). Subsequently, the assembly was cured in a 70 °C oven to form a soft, smooth protective layer.

Antimicrobial activity against planktonic cells

The microbial suspension at approximately 10^7 CFU/mL in PBS was added to 35 mm Petri dishes together with various volumes of F-gel (TQ concentration, 500 µg/mL) to explore a final concentration of TQ at 25, 50, 75 and 100 µg/mL in solution and incubated for 20 min, followed by bLED illumination at the bottom of the dish while stirring at 60 rpm. Aliquots of 50 µL of the suspensions were collected at 0, 2, 4, 6, 8 and 10 minutes, corresponding to 0, 6, 12, 18, 24 and 30 J/cm² bLED irradiation. Microbial activity was evaluated similarly with bLED or F-gel alone. Colony forming units (CFU) were determined by 10-fold serial dilution on BHI or YM agar plates, enumerated after 24 hours of culture and expressed as lg CFU/mL throughout the study, unless otherwise stated. The detection limit was 100 CFU/mL. SEM (JSM-7800F; JEOL) and TEM (Talos L120C G2, Thermo fisher) were used to observe the morphological alteration of microbes after combinatory treatment.

Bacterial transcriptome sequencing

A stationary phase culture of *Pa* was transferred to PBS and F-gel (TQ concentration, 500 µg/mL) solution to explore a final concentration of TQ at 100 µg/mL. The *Pa* was then exposed to sublethal doses of bLED for 5 min (50 mW, 15 J/cm²), followed by incubation for a further 2 h. Finally, the cells were harvested by centrifugation for high-throughput sequencing analysis.

Cell culture

HUVECs (catalog number:PCS-100-013), THP-1 (catalog number:TIB-202), and RAW264.7 (catalog number:TIB-71) cell lines were obtained from ATCC. HUVECs were cultured in Endothelial Cell Medium (ECM; ScienCell) supplemented with 10% Fetal Bovine Serum (FBS). RAW264.7 cells were maintained in Dulbecco's Modified Eagle's Medium (DMEM; Gibco) supplemented with 10% FBS, while THP-1 cells were cultured in RPMI 1640 medium (Gibco) supplemented with 10% FBS.

Cellular NAD(H), CIV activity and ATP level assays

HUVECs or THP-1 cells were seeded into a 24-well plate at a density of 2×10^5 cells per well and cultured overnight. Following this, the cells were treated with F-gel (NADH concentration, 100 µM) in one-tenth the volume of culture medium, rLED, or a combination of F-gel and rLED for 2 hours prior to being incubated with LPS (100 ng/mL) for 12 h. Subsequently, the cells were washed with PBS three times and lysed using 100 µL of lysis buffer. The cellular NAD(H) level and NAD⁺/NADH ratio were assessed using the NAD/NADH assay kit (ab65348, Abcam), cellular ATP levels were tested using a luminescent ATP detection kit (ab113849, Abcam), and cellular Complex IV activity was assessed with Complex IV enzyme activity microplate assay (ab109909, Abcam).

Measurement of inflammation-related cytokine levels

THP-1 or RAW264.7 cells were plated into a 96-well plate at a density of 2×10^4 cells per well and subjected to the treatments described above. After 24 hours of treatment, the cell culture media were collected to assess cytokine production using ELISA kits obtained from Thermo Fisher Scientific, following the manufacturer's instructions. Data were obtained by measuring the absorbance difference at 450 nm using a Microplate Reader.

In vitro macrophage phenotype regulation

THP-1 and Raw 264.7 cells were inoculated in 12-well plates and incubated at 37 °C with 5% CO₂ for 24 h. After that, cells were subjected to

the treatments described above and incubated with LPS (100 ng/mL) for 24 hours. Subsequently, the cells were stained with PE-labeled anti-CD86 antibody and APC-labeled anti-CD86 antibody according to the manufacturer's instructions, and then analyzed by flow cytometry.

In vivo infected diabetic mouse wound healing study

All procedures for the in vivo diabetic mouse skin wound healing study were approved by Shanghai Jiao Tong University Institutional Animal Care and Use Committee (IACUC). Male BALB/c mice (6 weeks old) were obtained from Slac biotechnology. The mice were housed in an environment with a temperature range of 24 °C to 26 °C, a relative humidity of 60% to 70%, and a light/dark cycle of 12 hours each. To establish the diabetic mouse model, mice were injected intraperitoneally (*i.p.*) with streptozotocin (STZ) at a dose of 50 mg/kg for five consecutive days. Blood glucose levels of the mice were monitored using a glucometer after cut the tail tip of the mouse to measure its random blood glucose. Mice with blood glucose levels <16.7 mM were excluded, and the remaining mice were confirmed as diabetic mice.

Diabetic mice were anesthetized using isoflurane, and a round wound with a diameter of 7 mm was created on the back of each mouse using a peeler. 50 µL of bioluminescent MRSA or *Pa* at a concentration of 1×10^9 CFUs per mL was then applied onto the wound to induce diabetic skin infection. Concurrently, the mice were divided into five groups: G1, control; G2, F-gel (NADH concentration, 100 µM; TQ concentration, 200 µg/mL); G3, rLED+F-gel; G4, bLED+F-gel; G5, r&bLED +F-gel. At day 2, after anesthesia, 100 µL F-gels were sprayed onto the wounds of groups G2, G3, G4, and G5 using a dual-cartridge sprayer and incubated for 20 min. Mice in G3 were irradiated with rLED (630 nm, 10 mW/cm²) for 5 min with LED patches covered on the wound. For groups G4 and G5, the mice were irradiated with bLED (470 nm, 50 mW/cm²) for 12 min using LED patches. After 30 min, mice in G5 were irradiated with rLED (630 nm, 10 mW/cm²) for 5 min. The patch was removed after treatment. Bacterial bioluminescence was acquired (10 s exposure, medium binning) at various times after treatment initiation using a Lumina in vivo imaging system (IVIS, PerkinElmer). In addition, exudate samples were collected from each wound by gently swabbing the wound with a sterile cotton swab, ensuring minimal disruption to the wound bed. The exudate was immediately transferred to sterile microcentrifuge tubes containing 1 mL of sterile saline, vortexed briefly for homogeneity, and then serially diluted in sterile saline (1:10, 1:100, 1:1000, etc.) to achieve countable colony ranges and then inoculated onto a bacterial culture dish for overnight incubation. Treatments and bacterial bioluminescence detection were performed every 2 days after anesthesia until day 8, and wounds were photographed every 4 days, with the length and width recorded to calculate the area. Representative mice from each group were sacrificed on days 8 and 16, and the wounded skin was collected for histological and immunofluorescent staining.

In vivo infected porcine skin wound healing study

All procedures were approved by IACUC at Shanghai Jiao Tong University. Two Panama minipigs weighing 12–15 kg were utilized for the study. Prior to modeling, the minipigs were acclimatized for 7 days. STZ (150 mg/kg) was then injected intravenously to induce diabetes, and fasting blood glucose was measured twice via ear vein to confirm the success of the model (blood glucose levels ≥ 16.7 mM). During the wound creation experiment, the back hair of the minipigs was removed, and the back sites were disinfected with iodophor and 70% ethanol. Subsequent operations were conducted under general anesthesia. Twenty full-thickness wounds with a diameter of 15 mm were created using a peeler, with 10 wounds on each side of the minipigs, maintaining a distance of 2 cm between two wounds. Subsequently, 100 µL of MRSA suspension at a concentration of 1×10^9 CFUs per mL was applied onto each wound to induce diabetic skin infection.

Simultaneously, the wounds were divided into five groups: G1, control; G2, F-gel (NADH concentration, 100 μ M; TQ concentration, 200 μ g/mL); G3, rLED+F-gel; G4, bLED+F-gel; G5, r&bLED+F-gel.

At day 2, 200 μ L F-gels were sprayed onto the wounds of groups G2, G3, G4, and G5 using a dual-cartridge sprayer and incubated for 20 min. Wounds in G3 were irradiated with rLED (630 nm, 10 mW/cm²) for 5 minutes with LED patches covered on the wound. For groups G4 and G5, the wounds were irradiated with bLED (470 nm, 50 mW/cm²) for 12 min using LED patches. After 30 minutes, mice in G5 were irradiated with rLED (630 nm, 10 mW/cm²) for 5 minutes. The patch was removed after treatment and 3 M™ Tegaderm™ transparent dressing was applied to cover the wounds, secured with skin staples. Additionally, the wound area was covered with sterile cotton gauze for further support and protection.

Following the procedures, the minipigs were monitored for any signs of discomfort and provided with feed and water. Each minipig was housed individually and monitored daily. Treatments were administered every four days. Wound images were captured every 4 days. At scheduled intervals, the minipigs were euthanized, and the wound tissues were harvested for further histological analysis.

Histological analysis

Wound tissues were collected at day 8 and day 16 after model induction and fixed in 4% paraformaldehyde (wound tissue from mice) or neutral formalin (wound tissue from minipigs). Subsequently, the tissues were embedded in paraffin wax and sliced into 5 μ m sections for subsequent H&E staining, Masson's trichrome staining (MTTS), and immunofluorescence staining.

For H&E and immunofluorescence staining, standard protocols provided by the manufacturer were followed. Sections were deparaffinized in xylene and rehydrated in graded ethanol. After microwaving in 10 mM sodium citrate, sections were incubated with primary antibodies overnight at 4 °C, followed by incubation with secondary antibodies for 30 minutes at 37 °C. Wound tissues were fixed in 4% formaldehyde for paraffin embedding. Tissue sections (5 μ m) were mounted on slides for histological analysis. H&E staining was performed to measure wound closure areas. MTTS was utilized to quantify collagen deposition. Immunofluorescence staining for CD86 and CD206 was conducted on days 8 and 16 after model establishment to observe macrophage infiltration and differentiation at the wound site.

Transcriptome analysis

Wound tissues obtained from diabetic mice and minipigs on day 8 were subjected to RNA extraction using TRIzol reagent (Invitrogen). The quality of RNA was assessed by measuring the A260/A280 ratio using a Nanodrop™ One spectrophotometer (Thermo Fisher Scientific Inc., USA), and the quantity was determined using Qubit 3.0 with a Qubit™ RNA Broad Range Assay kit (Thermo Fisher Scientific Inc., USA). For library preparation, 2 μ g of total RNA was treated with the Ribo-off rRNA Depletion Kit (Human/Mouse/Rat) (Illumina, USA) and then subjected to stranded RNA sequencing library preparation using the KCTM Stranded mRNA Library Prep Kit for Illumina (Wuhan Seq-Health Co., Ltd. China), following the manufacturer's protocols. The library products ranging from 200 to 500 bp were enriched, quantified, and sequenced using a NovaSeq 6000 sequencer (Illumina, USA) with the PE150 model.

RNA-seq data analysis was conducted using bioinformatics tools. Differential expression analysis was performed using the edge R software. Heatmaps were generated using the TBtools software (<https://github.com/CJ-Chen/TBtools/releases>). Gene Ontology (GO) terms and Kyoto Encyclopedia of Genes and Genomes (KEGG) pathways were identified using KOBAS 2.0. Hypergeometric tests and Benjamini–Hochberg false discovery rate (FDR) control procedures were employed to determine the enrichment of each term.

Statistical analysis

GraphPad Prism (version 9.50) was used to analyze the statistical significance of all comparative studies in this research. Normality of data distribution was assumed for parametric tests without formal testing. Group comparisons were conducted utilizing one-way ANOVA alongside Tukey's multiple comparison test. Statistical significance was acknowledged at $P < 0.05$ for all analysis.

Reporting summary

Further information on research design is available in the Nature Portfolio Reporting Summary linked to this article.

Data availability

The main data supporting the results in this study are available within the paper and its Supplementary Information. Data underlying Fig. 1–9 and Supplementary Figs 1–30 are provided with this paper in the Source Data file. The raw sequence data have been submitted to the NCBI Short Read Archive (SRA) with bioproject accession number PRJNA1170018. Any additional requests for information can be directed to, and will be fulfilled by, the corresponding authors. Source data are provided with this paper.

References

- Armstrong, D. G., Tan, T. W., Boulton, A. J. M. & Bus, S. A. Diabetic Foot Ulcers: A Review. *JAMA* **330**, 62–75 (2023).
- Mizelle, R. M. Jr. Diabetes, race, and amputations. *Lancet* **397**, 1256–1257 (2021).
- Uberoi, A., McCready-Vangi, A. & Grice, E. A. The wound microbiota: microbial mechanisms of impaired wound healing and infection. *Nat Rev Microbiol* (2024).
- Kalan, L. R. et al. Strain- and Species-Level Variation in the Microbiome of Diabetic Wounds Is Associated with Clinical Outcomes and Therapeutic Efficacy. *Cell Host Microbe* **25**, 641–655.e645 (2019).
- Grennan, D. Diabetic Foot Ulcers. *JAMA* **321**, 114 (2019).
- Rooke, L. S. J. et al. The challenge of antimicrobial resistance: What economics can contribute. *Science* **364** (2019).
- Brown, E. D. & Wright, G. D. Antibacterial drug discovery in the resistance era. *Nature* **529**, 336–343 (2016).
- Knipper, J. A., Ding, X. & Eming, S. A. Diabetes Impedes the Epigenetic Switch of Macrophages into Repair Mode. *Immunity* **51**, 199–201 (2019).
- Ye, M. et al. NAD(H)-loaded nanoparticles for efficient sepsis therapy via modulating immune and vascular homeostasis. *Nat. Nanotechnol.* **17**, 880–890 (2022).
- Huang, J. et al. A click chemistry-mediated all-peptide cell printing hydrogel platform for diabetic wound healing. *Nat. Commun.* **14**, 7856 (2023).
- Xiong, Y. et al. A Whole-Course-Repair System Based on Neurogenesis-Angiogenesis Crosstalk and Macrophage Reprogramming Promotes Diabetic Wound Healing. *Adv. Mater.* **35**, e2212300 (2023).
- Lu, M. et al. Bacteria-specific phototoxic reactions triggered by blue light and phytochemical carvacrol. *Sci. Transl. Med.* **13** (2021).
- Leanse, L. G., Dos Anjos, C., Mushtaq, S. & Dai, T. Antimicrobial blue light: A 'Magic Bullet' for the 21st century and beyond? *Adv. Drug Deliv. Rev.* **180**, 114057 (2022).
- Zhao, C. et al. Transcranial photobiomodulation enhances visual working memory capacity in humans. *Sci. Adv.* **8**, eabq3211 (2022).
- Sim, J. H. et al. OLED catheters for inner-body phototherapy: A case of type 2 diabetes mellitus improved via duodenal photobiomodulation. *Sci. Adv.* **9**, eadh8619 (2023).
- Lee, G.-H. et al. Multifunctional materials for implantable and wearable photonic healthcare devices. *Nat. Rev. Mater.* **5**, 149–165 (2020).

17. Zhang, Z., Wang, Y., Jia, S. & Fan, C. Body-conformable light-emitting materials and devices. *Nat. Photonics* **18**, 114–126 (2024).
18. Katiyar, A. K. et al. 2D Materials in Flexible Electronics: Recent Advances and Future Prospectives. *Chem. Rev.* **124**, 318–419 (2024).
19. Kang, J., Tok, J. B.-H. & Bao, Z. Self-healing soft electronics. *Nat. Electron.* **2**, 144–150 (2019).
20. Ryu, J. E. et al. Technological Breakthroughs in Chip Fabrication, Transfer, and Color Conversion for High-Performance Micro-LED Displays. *Adv. Mater.* **35**, 2204947 (2023).
21. Hong, G. et al. A Brief History of OLEDs-Emitter Development and Industry Milestones. *Adv. Mater.* **33**, e2005630 (2021).
22. Jang, E. & Jang, H. Quantum dot light-emitting diodes. *Chem. Rev.* **123**, 4663–4692 (2023).
23. Yang, S. et al. Research progress in hybrid light-emitting diodes based on quantum dots and organic emitters. *J. Luminesci.* 120560 (2024).
24. Kim, J. S. et al. Ultra-bright, efficient and stable perovskite light-emitting diodes. *Nature* **611**, 688–694 (2022).
25. Anwar, A. R. et al. Recent progress in micro-LED-based display technologies. *Laser Photonics Rev.* **16**, 2100427 (2022).
26. Tankelevičiūtė, E., Samuel, I. D. & Zysman-Colman, E. The Blue Problem: OLED Stability and Degradation Mechanisms. *J. Phys. Chem. Lett.* **15**, 1034–1047 (2024).
27. Kim, J. et al. Critical role of electrons in the short lifetime of blue OLEDs. *Nat. Commun.* **14**, 7508 (2023).
28. Bourget, C. M. An introduction to light-emitting diodes. *HortScience* **43**, 1944–1946 (2008).
29. Galyanin, V., Belikov, V., Belikova, V. & Bogomolov, A. Emission band width approximation of light-emitting diodes in the region 350–2100 nm. *Sens. Actuators B: Chem.* **252**, 773–776 (2017).
30. Dodd, E. M., Winter, M. A., Hordinsky, M. K., Sadick, N. S. & Farah, R. S. Photobiomodulation therapy for androgenetic alopecia: A clinician's guide to home-use devices cleared by the Federal Drug Administration. *J. Cosmet. Laser Ther.* **20**, 159–167 (2018).
31. Lee, S. Y. et al. Combinatorial wound healing therapy using adhesive nanofibrous membrane equipped with wearable LED patches for photobiomodulation. *Sci. Adv.* **8**, eabn1646 (2022).
32. Hu, X. et al. Stretchable inorganic-semiconductor electronic systems. *Adv. Mater.* **23**, 2933–2936 (2011).
33. Morikawa, Y., Ayub, S., Paul, O., Kawano, T. & Ruther, P. in 2019 20th International Conference on Solid-State Sensors, Actuators and Microsystems & Eurosensors XXXIII (TRANSDUCERS & EUROSENSORS XXXIII) 2484–2487 (IEEE, 2019).
34. Jiang, Y. et al. Wireless, closed-loop, smart bandage with integrated sensors and stimulators for advanced wound care and accelerated healing. *Nat. Biotechnol.* **41**, 652–662 (2023).
35. Chen, Q. et al. In situ sprayed bioresponsive immunotherapeutic gel for post-surgical cancer treatment. *Nat. Nanotechnol.* **14**, 89–97 (2019).
36. Ouyang, J. et al. In situ sprayed NIR-responsive, analgesic black phosphorus-based gel for diabetic ulcer treatment. *Proc. Natl Acad. Sci. USA* **117**, 28667–28677 (2020).
37. Li, Y. et al. Injectable hydrogel with MSNs/microRNA-21-5p delivery enables both immunomodification and enhanced angiogenesis for myocardial infarction therapy in pigs. *Sci. Adv.* **7** (2021).
38. Jin, L. et al. Microenvironment-Activated Nanozyme-Armed Bacteriophages Efficiently Combat Bacterial Infection. *Adv. Mater.* **35**, e2301349 (2023).
39. Guo, J. et al. 9,10-Phenanthrenequinone: A Promising Kernel to Develop Multifunctional Antitumor Systems for Efficient Type I Photodynamic and Photothermal Synergistic Therapy. *ACS Nano* **15**, 20042–20055 (2021).
40. Kang, M. et al. Good Steel Used in the Blade: Well-Tailored Type-I Photosensitizers with Aggregation-Induced Emission Characteristics for Precise Nuclear Targeting Photodynamic Therapy. *Adv. Sci. (Weinh.)* **8**, e2100524 (2021).
41. Yamada, M. & Sakai, H. Hidden Antioxidative Functions of Reduced Nicotinamide Adenine Dinucleotide Coexisting with Hemoglobin. *ACS Chem. Biol.* **12**, 1820–1829 (2017).
42. Gomez-Virgilio, L., Luarte, A., Ponce, D. P., Bruna, B. A. & Behrens, M. I. Analyzing Olfactory Neuron Precursors Non-Invasively Isolated through NADH FLIM as a Potential Tool to Study Oxidative Stress in Alzheimer's Disease. *Int. J. Mol. Sci.* **22** (2021).
43. Suthanthiran, M. et al. Hydroxyl radical scavengers inhibit human natural killer cell activity. *Nature* **307**, 276–278 (1984).
44. Ding, Q. et al. Oxidative Damage of Tryptophan Hydroxylase-2 Mediated by Peroxisomal Superoxide Anion Radical in Brains of Mouse with Depression. *J. Am. Chem. Soc.* **142**, 20735–20743 (2020).
45. Oliveira, N. M., Foster, K. R. & Durham, W. M. Single-cell twitching chemotaxis in developing biofilms. *Proc. Natl Acad. Sci. USA* **113**, 6532–6537 (2016).
46. Keegstra, J. M., Carrara, F. & Stocker, R. The ecological roles of bacterial chemotaxis. *Nat. Rev. Microbiol.* **20**, 491–504 (2022).
47. Oyeboode, O., Houreld, N. N. & Abrahamse, H. Photobiomodulation in diabetic wound healing: A review of red and near-infrared wavelength applications. *Cell Biochem Funct.* **39**, 596–612 (2021).
48. Zhang, Q., Dong, T., Li, P. & Wu, M. X. Noninvasive low-level laser therapy for thrombocytopenia. *Sci. Transl. Med.* **8**, 349ra101 (2016).
49. Maghfour, J. et al. Photobiomodulation CME Part I: Overview and Mechanism of Action. *J. Am. Acad. Dermatol.* (2024).
50. Meisel, J. D. et al. Hypoxia and intra-complex genetic suppressors rescue complex I mutants by a shared mechanism. *Cell* **187**, 659–675.e618 (2024).
51. Huang, Y. Y., Chen, A. C., Carroll, J. D. & Hamblin, M. R. Biphasic dose response in low level light therapy. *Dose Response* **7**, 358–383 (2009).
52. Arnaoutova, I. & Kleinman, H. K. In vitro angiogenesis: endothelial cell tube formation on gelled basement membrane extract. *Nat. Protoc.* **5**, 628–635 (2010).
53. Cameron, A. M. et al. Inflammatory macrophage dependence on NAD(+) salvage is a consequence of reactive oxygen species-mediated DNA damage. *Nat. Immunol.* **20**, 420–432 (2019).
54. Lv, Y. et al. YAP Controls Endothelial Activation and Vascular Inflammation Through TRAF6. *Circ. Res.* **123**, 43–56 (2018).
55. Eming, S. A., Wynn, T. A. & Martin, P. Inflammation and metabolism in tissue repair and regeneration. *Science* **356**, 1026–1030 (2017).
56. Willenborg, S. et al. Mitochondrial metabolism coordinates stage-specific repair processes in macrophages during wound healing. *Cell Metab.* **33**, 2398–2414.e2399 (2021).
57. Yang, X. et al. Excessive nucleic acid R-loops induce mitochondria-dependent epithelial cell necroptosis and drive spontaneous intestinal inflammation. *Proc. Natl Acad. Sci. USA* **121**, e2307395120 (2024).
58. Lu, G. et al. Myeloid cell-derived inducible nitric oxide synthase suppresses M1 macrophage polarization. *Nat. Commun.* **6**, 6676 (2015).
59. Deng, T. et al. A natural biological adhesive from snail mucus for wound repair. *Nat. Commun.* **14**, 396 (2023).
60. Matoori, S., Veves, A. & Mooney, D. J. Advanced bandages for diabetic wound healing. *Sci. Transl. Med.* **13** (2021).
61. Eming, S. A., Murray, P. J. & Pearce, E. J. Metabolic orchestration of the wound healing response. *Cell Metab.* **33**, 1726–1743 (2021).
62. Konieczny, P. et al. Interleukin-17 governs hypoxic adaptation of injured epithelium. *Science* **377**, eabg9302 (2022).
63. Summerfield, A., Meurens, F. & Ricklin, M. E. The immunology of the porcine skin and its value as a model for human skin. *Mol. Immunol.* **66**, 14–21 (2015).
64. Verma, K. D., Lewis, F., Mejia, M., Chalasani, M. & Marcus, K. A. Food and Drug Administration perspective: Advancing product

- development for non-healing chronic wounds. *Wound Repair Regen.* **30**, 299–302 (2022).
65. Sen, C. K. Human Wound and Its Burden: Updated 2022 Compendium of Estimates. *Adv. Wound Care (N. Rochelle)* **12**, 657–670 (2023).
 66. Tecilazich, F., Dinh, T. L. & Veves, A. Emerging drugs for the treatment of diabetic ulcers. *Expert Opin. Emerg. Drugs* **18**, 207–217 (2013).
 67. Bowling, F. L., Rashid, S. T. & Boulton, A. J. Preventing and treating foot complications associated with diabetes mellitus. *Nat. Rev. Endocrinol.* **11**, 606–616 (2015).
 68. Zhang, J. et al. An Electroluminodynamic Flexible Device for Highly Efficient Eradication of Drug-Resistant Bacteria. *Adv. Mater.* **34**, e2200334 (2022).
 69. He, Y. et al. A multifunctional hydrogel coating to direct fibroblast activation and infected wound healing via simultaneously controllable photobiomodulation and photodynamic therapies. *Biomaterials* **278**, 121164 (2021).
 70. Xiong, Z. et al. A wireless and battery-free wound infection sensor based on DNA hydrogel. *Sci. Adv.* **7**, eabj1617 (2021).
 71. Yang, L. et al. Biofilm microenvironment triggered self-enhancing photodynamic immunomodulatory microneedle for diabetic wound therapy. *Nat. Commun.* **14**, 7658 (2023).
 72. Xiu, W. et al. Biofilm Microenvironment-Responsive Nanotheranostics for Dual-Mode Imaging and Hypoxia-Relief-Enhanced Photodynamic Therapy of Bacterial Infections. *Res. (Wash. D. C.)* **2020**, 9426453 (2020).
 73. Liang, W. et al. Peroxisome proliferator-activated receptor- α (PPAR α) regulates wound healing and mitochondrial metabolism in the cornea. *Proc. Natl Acad. Sci. USA* **120**, e2217576120 (2023).
 74. Qi, W. et al. Pyruvate kinase M2 activation may protect against the progression of diabetic glomerular pathology and mitochondrial dysfunction. *Nat. Med.* **23**, 753–762 (2017).
 75. Hunt, M., Torres, M., Bachar-Wikstrom, E. & Wikstrom, J. D. Multifaceted roles of mitochondria in wound healing and chronic wound pathogenesis. *Front Cell Dev. Biol.* **11**, 1252318 (2023).
 76. Levoux, J. et al. Platelets Facilitate the Wound-Healing Capability of Mesenchymal Stem Cells by Mitochondrial Transfer and Metabolic Reprogramming. *Cell Metab.* **33**, 283–299.e289 (2021).
 77. Fu, H. et al. Wounding triggers MIRO-1 dependent mitochondrial fragmentation that accelerates epidermal wound closure through oxidative signaling. *Nat. Commun.* **11**, 1050 (2020).
 78. de Freitas, L. F. & Hamblin, M. R. Proposed Mechanisms of Photobiomodulation or Low-Level Light Therapy. *IEEE J Sel Top Quant. Electr.* **22** (2016).

Acknowledgements

This work was supported by the National Key R&D Program of China (2020YFC1512704) and the Comprehensive Planning Bureau of Logistics Support Department of the Military Commission (CZZ8J010) to M.Y., National Natural Science Foundation of China (82002188), Natural Science Foundation of Shanghai (23ZR1456800), Interdisciplinary Program of Shanghai Jiao Tong University (YG2021ZD07), and Shanghai Municipal Health Commission General Project (202240185) to M.L. (Min Lu). We

thank the Instrumental Analysis Center of Shanghai Jiao Tong University for their support with the relevant tests in this paper.

Author contributions

M.L. (Ming Li), C.W., Y.M. and M.L. (Min Lu) designed the study. M.L. (Ming Li), C.W. and M.L. (Min Lu) conceived the idea and developed the materials and method for the r&bLED and F-gel. M.L. (Ming Li), M.W., M.Y. and M.L. (Min Lu) designed the in vitro and ex vivo experiment. M.L. (Ming Li), C.W., Q.Y., H.C. and Y.M. conducted the in vitro and ex vivo experiment and analysis. M.L. (Ming Li), Y.M., and L.W. designed and conducted the in vivo diabetic mouse wound healing experiment and analysis. M.L. (Ming Li), C.W., Y.M. and L.W. designed and conducted the in vivo diabetic porcine wound healing experiment. M.L. (Ming Li) completed the flow cytometry, histology, immunofluorescence and sequencing analysis. C.W. performed histology assessment and scoring. M.L. (Ming Li), C.W., Q.Y. and H.C. prepared the figures. M.L. (Ming Li), M.W., M.Y. and M.L. (Min Lu) wrote the manuscript with inputs from all authors.

Competing interests

The authors declare no competing interests.

Additional information

Supplementary information The online version contains supplementary material available at <https://doi.org/10.1038/s41467-024-53579-6>.

Correspondence and requests for materials should be addressed to Mei X. Wu, Min Yao or Min Lu.

Peer review information *Nature Communications* thanks Yongmin Jeon, and the other, anonymous, reviewer(s) for their contribution to the peer review of this work. A peer review file is available.

Reprints and permissions information is available at <http://www.nature.com/reprints>

Publisher's note Springer Nature remains neutral with regard to jurisdictional claims in published maps and institutional affiliations.

Open Access This article is licensed under a Creative Commons Attribution-NonCommercial-NoDerivatives 4.0 International License, which permits any non-commercial use, sharing, distribution and reproduction in any medium or format, as long as you give appropriate credit to the original author(s) and the source, provide a link to the Creative Commons licence, and indicate if you modified the licensed material. You do not have permission under this licence to share adapted material derived from this article or parts of it. The images or other third party material in this article are included in the article's Creative Commons licence, unless indicated otherwise in a credit line to the material. If material is not included in the article's Creative Commons licence and your intended use is not permitted by statutory regulation or exceeds the permitted use, you will need to obtain permission directly from the copyright holder. To view a copy of this licence, visit <http://creativecommons.org/licenses/by-nc-nd/4.0/>.

© The Author(s) 2024